CrossMark

The strength of the tropical inversion and its response to climate change in 18 CMIP5 models

Xin Qu · Alex Hall · Stephen A. Klein · Peter M. Caldwell

Abstract We examine the tropical inversion strength, measured by the estimated inversion strength (EIS), and its response to climate change in 18 models associated with phase 5 of the coupled model intercomparison project (CMIP5). While CMIP5 models generally capture the geographic distribution of observed EIS, they systematically underestimate it off the west coasts of continents, due to a warm bias in sea surface temperature. The negative EIS bias may contribute to the low bias in tropical low-cloud cover in the same models. Idealized perturbation experiments reveal that anthropogenic forcing leads directly to EIS increases, independent of "temperature-mediated" EIS increases associated with long-term oceanic warming. This fast EIS response to anthropogenic forcing is strongly impacted by nearly instantaneous continental warming. The temperature-mediated EIS change has contributions from both uniform and non-uniform oceanic warming. The substantial EIS increases in uniform oceanic warming simulations are due to warming with height exceeding the moist adiabatic lapse rate in tropical warm pools. EIS also increases in fully-coupled ocean–atmosphere simulations where CO_2 concentration is instantaneously quadrupled, due to both fast and temperature-mediated changes. The temperature-mediated EIS change varies with tropical warming in a nonlinear fashion: The EIS change per degree tropical warming is much larger in the early stage of the simulations than in the late stage, due to delayed warming in the eastern parts of the subtropical oceans. Given the importance of EIS in regulating tropical low-cloud cover, this suggests that the tropical low-cloud feedback may also be nonlinear.

Keywords Tropical inversion · EIS · Fast response · Temperature-mediated change

1 Introduction

The lowest few kilometers of the tropical marine atmosphere are frequently capped by an inversion layer, characterized by a large temperature and/or moisture jump. Under this inversion lie several types of boundary layer clouds (Klein and Hartmann 1993; Betts 1997; Moeng and Stevens 1999; Stevens 2005; Wood 2012). Through their effect on net incoming shortwave radiation, these clouds play a critical role in regulating the global energy budget (Hartmann et al. 1992; Chen et al. 2000). Changes in these clouds associated with simulated anthropogenic climate change likewise have a large effect on the shortwave component of the anthropogenic perturbation to the global energy budget (Slingo 1990; Bony and Dufresne 2005; Stephens 2005; Soden and Held 2006; Williams et al. 2006; Wyant et al. 2006; Webb et al. 2012; Zelinka et al. 2012). These changes remain the major source of uncertainty surrounding climate sensitivity (Webb et al. 2012; Vial et al. 2013).

A key factor controlling the amount of low clouds in the observed climate is the strength of the inversion. A stronger inversion suppresses the mixing of boundary layer air with warmer and drier air in the free-troposphere, leading to a shallower, moister and cloudier boundary layer. In

X. Qu (✉) · A. Hall
Department of Atmospheric and Oceanic Sciences,
University of California, PO Box 951565, Los Angeles,
CA 90095-1565, USA
e-mail: xinqu@atmos.ucla.edu

S. A. Klein · P. M. Caldwell
Program for Climate Model Diagnosis and Intercomparison,
Lawrence Livermore National Laboratory, Mail Code L-103,
PO Box 808, Livermore, CA 94551, USA

Table 1 Eighteen CMIP5 models used in this study

Model	Hist/RCP8.5	amip	amip4xCO2/amip4K/ amipFuture/sstClim/ sstClim4xCO2	aquaControl/ aqua4xCO2/ aqua4K	LGM	piControl/ abrupt4xCO2
BCC-CSM1.1	X	X*	X*			X
CCSM4	X	X	X	X	X	X
CSIRO-Mk3.6	X	X				X
CanESM2	X	X	X			X
FGOALS-s2	X*	X				X
GFDL-CM3	X	X				X
GFDL-ESM2G	X					X
GFDL-ESM2M	X					X
GISS-E2-R	X	X				X
HadGEM2-CC	X					
HadGEM2-ES	X	X	X	X		X
IPSL-CM5A-LR	X	X	X	X	X*	X
MIROC-ESM	X				X	X
MIROC-ESM-CHEM	X					
MIROC5	X	X	X	X		X
MPI-ESM-LR	X*	X*	X*	X*		X*
MRI-CGCM3	X	X	X	X	X	X
NorESM1-M	X	X				X

1st column: Names of the models. 2nd–7th columns: The availability of different simulations. A number of simulations (identified by the asterisk) do not provide surface relative humidity data. They are not used in the calculations in Appendix 3

the absence of detailed balloon soundings over large space and time scales, the inversion has been traditionally measured by the difference in potential temperature between 700 hPa and the surface (termed the lower-troposphere stability, LTS), but more recently the estimated inversion strength (EIS, Wood and Bretherton 2006). There is ample observational evidence for a link between inversion strength and low-cloud cover (LCC). Seasonal and interannual LCC variations in many low cloud regions are strongly associated with variations in this quantity (Slingo 1980; Klein and Hartmann 1993; Wood and Bretherton 2006; Zhang et al. 2009; Sun et al. 2011; Kubar et al. 2012; Qu et al. 2014).

Given the importance of the tropical inversion to LCC, it is natural to ask whether climate models participating in phase 5 of the coupled model intercomparison project (CMIP5) can simulate it faithfully. Many fully coupled ocean–atmosphere model simulations exhibit a warm bias in sea surface temperature (SST) at the west coasts of subtropical continents (Zheng et al. 2011; Xu et al. 2013). Assuming no similar warm bias occurs in the free troposphere, this bias would translate into a negative bias in the inversion strength. This negative bias, where present, would lead to a similar bias in LCC in coupled simulations. In this study, we assess the realism of the tropical inversion simulated in 18 CMIP5 models (see Table 1) against reanalysis.

It is also of great interest to investigate the response of inversion strength to anthropogenic forcing. Several recent studies suggested that EIS would increase in a warming climate (Caldwell et al. 2012; Watanabe et al. 2012; Webb et al. 2012; Ogura et al. 2013; Qu et al. 2014). Qu et al. (2014) attributed this increase to the fact that the air above the boundary layer warms more than would be predicted by a local moist adiabat. Furthermore, Webb et al. (2012) showed that a simulated EIS increase can be broken down into two components—one associated with a fast response (FR) to anthropogenic forcing, and the other a slow warming (i.e., the temperature-mediated component).

In this study, we further our understanding of future EIS change by exploiting a variety of climate perturbation experiments in the CMIP5 archive. Specifically, we address four questions as folllows. First, how large is the fast EIS change simulated by CMIP5 models? We compute the fast EIS change based on CO_2 quadrupling simulations done with atmospheric general circulation models (AGCMs). Note that Webb et al. (2012) used slab-ocean models participating in phase 3 of the coupled model intercomparison project (CMIP3), which may or may not give different results for simulated fast EIS change.

Second, what drives the temperature-mediated EIS change? Qu et al. (2014) attributed it in part to nonuniform oceanic warming (NOW), i.e., the fact that warming in tropical warm

pools is greater than warming in low cloud regions (Qu et al. 2014). The underlying argument for this is the following: Free tropospheric tropical temperatures are largely set by SST in the warm pools. So if the warm pool SST increases by more than the SST in the low-cloud regions, then the free tropospheric temperature warming in the subsidence regions will exceed that predicted by a local moist adiabat and hence there will be an EIS increase in the low cloud regions. However, it is unclear what fraction of simulated EIS change is attributable to NOW, as opposed to a generally warming climate, or whether uniform oceanic warming (UOW) does not drive any EIS change, as hypothesized by Wood and Bretherton (2006). To assess these issues, we first examine the impact of UOW on EIS using AGCM experiments with imposed uniform SST warming of 4K, and then, we quantify the impact of NOW on EIS using AGCM experiments with imposed SST warming pattern. If UOW does not contribute to any EIS change, then we conclude that the temperature-mediated EIS change is induced by NOW alone. Otherwise, both UOW and NOW contribute to the temperature-mediated EIS change.

Third, does warming over tropical land play a significant role in driving EIS change in the tropical ocean? Qu et al. (2014) hypothesized that the rapid warming over land could enhance free-tropospheric warming over ocean through tropical circulation, contributing to a EIS increase. We address this question by comparing EIS change in AGCM simulations with an aqua planet configuration to those seen in AGCM simulations with a realistic land configuration. Since many experiments with CO_2 quadrupling or uniform SST warming were done with both configurations, we can assess the role of the continental warming in both the fast and UOW-driven EIS changes.

Finally, how do individual components of EIS change (FR, UOW and NOW) manifest themselves in fully-coupled ocean–atmosphere simulations? We first examine the EIS change in two types of warming experiments done with coupled models (abrupt4xCO2 and RCP8.5). To investigate whether changes in the tropical inversion are symmetric with respect to the sign of climate change, we also examine the EIS change in coupled model simulations for the Last Glacial Maximum (LGM), a period substantially cooler than present day. Lastly, we quantify the respective contributions of FR, UOW and NOW to the various EIS changes.

The study is presented as follows: Data and methodology are described in Sect. 2. In this section, we also provide a brief derivation of EIS as in Wood and Bretherton (2006) and re-introduce the simple expression for EIS change derived in Qu et al. (2014). We assess simulated present-day tropical inversion against reanalysis in Sect. 3. EIS changes in various idealized AGCM simulations are examined in Sect. 4, and EIS changes in coupled model simulations are examined in Sect. 5. A summary and discussion are found in Sect. 6.

2 Data and methodology

2.1 Data

Present-day (1979–2008) tropical inversion simulated by 18 coupled models and 13 AGCMs (Table 1) are examined. In the coupled model simulations, historical forcing was imposed in the 20th-century, which end in 2005, while the Representative Concentration Pathway (RCP) 8.5 was imposed from 2006 onward (Taylor et al. 2012). Note that to compute the present-day EIS, we utilize both historical and RCP8.5 simulations. In the AGCM simulations (amip), observed CO_2 concentration and SST were imposed. Because there are no detailed balloon soundings over the large space of the tropical ocean and because satellite observation is subject to large sampling bias (Yue et al. 2011), we use reanalysis to assess the realism of the tropical inversion in models. To explore the uncertainty in reanalysis, we use three different reanalysis data sets—ERA-Interim (Dee et al. 2011), NCAR/NCEP (Kalnay et al. 1996) and MERRA (Rienecker et al. 2011).

To investigate the response of the tropical inversion to anthropogenic forcing, we examine a variety of climate perturbation experiments done with either AGCMs or coupled models (see Table 1). The configurations of the simulations are briefly described in Table 2 (see Taylor et al. 2012 for detail). While this study is concerned with the tropical inversion in general, additional attention is given to five subtropical oceanic regions dominated by stratocumulus clouds, defined by black boxes in Fig. 1. These five regions have been studied extensively (Klein and Hartmann 1993; Wood and Bretherton 2006; Zhang et al. 2009; Caldwell et al. 2012, referred hereafter to as the KH domains). Results in this study are based on annually averaged data. For reference, all acronyms used in this paper are listed in Table 3.

2.2 Defining EIS

EIS is defined as in Wood and Bretherton (2006):

$$EIS = LTS - \Gamma_m^{850} \cdot (z_{700} - LCL) \tag{1}$$

where LTS is the lower-tropospheric stability, Γ_m^{850} is the moist-adiabatic potential temperature gradient (Γ_m) at 850 hPa, which is a function of the in-situ temperature, z_{700} is the height of the 700 hPa surface, and LCL is the lifting condensation level. Consistent with Wood and Bretherton (2006), we approximate the 850 hPa temperature by averaging 700 hPa and surface temperatures. While Γ_m is actually a function of temperature and pressure, the single value used in Eq. (1) is applied to all heights between the LCL and z_{700}. (See Wood and Bretherton (2006) for a detailed derivation of EIS.) Due to this assumption, EIS is actually a slightly

Table 2 A brief description of the simulations used in this study

Simulation	Description
amip	AGCM simulations with observed CO_2 concentration and SST (1979–2008)
amip4xCO2	AGCM simulations with observed SST (1979–2008) and a CO_2 concentration four times the observed level (1979–2008)
amip4K	AGCM simulations with observed CO_2 concentration (1979–2008) and observed SST (1979–2008) plus a uniform 4K warming
amipFuture	AGCM simulations with observed CO_2 concentration (1979–2008) and observed SST (1979–2008) plus a prescribed SST anomaly pattern
sstClim	AGCM simulations with the pre-industrial SST and CO_2 concentration
sstClim4xCO2	AGCM simulations with the pre-industrial SST and a CO_2 concentration four times the pre-industrial level
aquaControl	Aqua planet AGCM simulations with prescribed SST and observed CO_2 concentration (1979–2008)
aqua4xCO2	Aqua planet AGCM simulations with prescribed SST and a CO_2 concentration four times the observed CO_2 level (1979–2008)
aqua4K	Aqua planet AGCM simulations with observed CO_2 concentration (1979–2008) and prescribed SST plus a uniform 4K warming
historical	Coupled ocean–atmosphere simulations with historical forcing imposed (1850–2005)
RCP8.5	Coupled ocean–atmosphere simulations with the Representative concentration pathway (RCP) 8.5 imposed (2006–2099)
piControl	Coupled ocean–atmosphere simulations with preindustrial forcing imposed
abrupt4xCO2	Coupled ocean–atmosphere simulations where CO_2 concentration is instantaneously quadrupled from the preindustrial level
LGM	Coupled ocean–atmosphere simulations with the Last Glacial Maximum conditions for ice sheets and CO_2 concentration

Table 3 A list of acronyms used in this paper

LTS	Lower-troposphere stability
EIS	Estimated inversion strength
LCC	Low cloud cover
CMIP	Coupled model intercomparison project
SST	Sea surface temperature
FR	Fast response
AGCM	Atmospheric general circulation model
NOW	Nonuniform oceanic warming
UOW	Uniform oceanic warming
RH_s	Surface relative humidity
LGM	Last glacial maximum
RCP	Representative concentration pathway
LCL	Lifting condensation level
KH	Klein and Hartmann
GHG	Greenhouse gas

biased measure of the inversion strength (see Appendix 1). However, we find that this bias is systematic and occurs in both current and future climates. Therefore, it has little effect on our estimated EIS change. Surface relative humidity (RH_s) is used in the *LCL* calculations. As in Wood and Bretherton (2006), it is fixed at 80 % in all EIS calculations except where the effect of simulated RH_s change on estimated EIS change is quantified in Appendix 3.

Based on Eq. (1) and using typical values for temperature, sea level pressure and RH_s (see Qu et al. 2014 for detail), we can express a given EIS change (ΔEIS) as a linear combination of temperature changes at 700 hPa (ΔT_{700}) and at the surface (ΔT_s):

$$\Delta EIS \approx \Delta T_{700} - 1.2\Delta T_s \qquad (2)$$

According to this simple expression, ΔEIS equals zero where $\Delta T_{700}/\Delta T_s \approx 1.2$. As expected from the definition of EIS, this condition is met if the vertical profile of tropospheric warming follows the moist adiabat from the surface, given surface warming. (See Appendix 1 for a demonstration of this point.) Therefore, we can interpret ΔEIS as the portion of ΔT_{700} that exceeds the moist adiabat. Qu et al. (2014) demonstrated that using Eq. (2) instead of (1) introduces very little error. In this paper, we use it as a tool to understand the sign and magnitude of ΔEIS, as well as its spatial distribution.

2.3 Computing various EIS changes

The EIS change due to FR ($\Delta EIS(FR)$) is computed based on CO_2 quadrupling simulations (amip4xCO2) done with 8 AGCMs and their corresponding control simulations (amip). These AGCMs are the atmospheric components of 8 fully coupled atmosphere-ocean models in the CMIP5 archive listed in Table 1. For convenience, we refer to them by their corresponding coupled models. To facilitate comparison, these AGCMs are also used to compute EIS changes in other perturbed AGCM simulations, and their corresponding coupled models are used to compute EIS changes in coupled model simulations. The fast EIS response is quantified by the difference in EIS climatologies between amip and amip4xCO2 simulations. To assess the sensitivity of $\Delta EIS(FR)$ to mean SST, we also quantify $\Delta EIS(FR)$ based on 8 sstClim4xCO2 simulations and their corresponding control simulations (sstClim). These simulations differ from their respective amip and amip4xCO2 simulations in the imposed SST values (see Table 2). We find that within each AGCM, $\Delta EIS(FR)$ based on the

sstClim and sstClim4xCO2 simulations differs little from $\Delta EIS(FR)$ based on the amip and amip4xCO2 simulations (not shown). Therefore, $\Delta EIS(FR)$ is not sensitive to the mean climate on which the CO_2 forcing is imposed. Lastly, we compute the fast EIS response in six AGCM simulations with an aqua planet configuration based on their respective aquaControl and aqua4xCO2 simulations (see Tables 1, 2). Comparison of the fast EIS response between AGCM simulations with an aqua planet configuration and those with a realistic land configuration allows us to assess the impact of the anthropogenically-forced continental warming on the fast EIS change in the tropical ocean.

The EIS change due to UOW ($\Delta EIS(UOW)$) is computed based on 8 uniform oceanic warming simulations (amip4K) and their corresponding amip simulations (see Tables 1, 2). The impact of UOW on EIS is quantified by the difference in EIS climatologies between amip and amip4K simulations. Similar procedures are also used to quantify $\Delta EIS(UOW)$ in six aqua planet AGCMs based on their respective aquaControl and aqua4K simulations (see Tables 1, 2). Comparison of $\Delta EIS(UOW)$ between the aqua planet AGCM simulations and those with a realistic land configuration allows us to assess the impact of the anthropogenically-forced continental warming on $\Delta EIS(UOW)$.

The EIS change due to NOW ($\Delta EIS(NOW)$) is computed based on 8 amipFuture simulations and their corresponding amip simulations (see Tables 1, 2). In the amipFuture simulations, AGCMs are forced by observed SST plus a prescribed SST anomaly pattern. The prescribed pattern was derived from a composite of SST change patterns simulated in several CMIP3 models at time of CO_2 quadrupling (Taylor et al. 2012). It was imposed in every amipFuture simulation. We diagnose $\Delta EIS(NOW)$ in two steps. First, we compute the EIS change between the amip and amipFuture simulations. Since the amipFuture simulations also include the impact of uniform oceanic warming, we then remove $\Delta EIS(UOW)$ from the resulting EIS change. Because warming in the tropical ocean differs little in the amip4K (4 K) and amipFuture simulations ($\sim$4.4 K), there is no need to rescale $\Delta EIS(UOW)$ beforehand.

We examine the evolution of the EIS change (ΔEIS (abrupt4xCO2)) in 8 abrupt4xCO2 simulations relative to their corresponding control simulations (piControl). Both types of simulations are done with coupled models (see Table 2). We construct the time series of annual-mean EIS change at each location for the duration (150 years) of abrupt4xCO2 simulations. It turns out that in most models, the tropical EIS change is a nonlinear function of warming (see Sect. 5). To understand this behavior, we examine two time periods in the simulations—the first and last 30 years. We quantify the average EIS change in these two periods, as well as its temperature-mediated component.

The EIS change in the 21st-century ($\Delta EIS(RCP8.5)$) is quantified by the difference in EIS climatologies between present-day (1979–2008) and future (2070–2099). These climatologies are taken from historical and RCP8.5 simulations done with 8 coupled models (Tables 1, 2). It turns out that $\Delta EIS(RCP8.5)$ bears great resemblance to the EIS change in the first 30 years of abrupt4xCO2 simulations. For this reason, we only touch upon $\Delta EIS(RCP8.5)$ in this paper. The EIS change in four LGM simulations ($\Delta EIS(LGM)$) is quantified by the difference in the EIS climatologies between present-day and LGM. The present-day EIS climatology is taken from historical and RCP8.5 simulations done with the four coupled models with available LGM simulations.

2.4 Decomposing EIS changes in the coupled model simulations

To better understand the EIS change in abrupt4xCO2 simulations, we decompose it into four components as follows

$$\Delta EIS = \alpha \cdot \Delta EIS(FR) + \beta \cdot \Delta EIS(UOW) \\ + \gamma \cdot \Delta EIS(NOW) + \Delta EIS(Res) \tag{3}$$

where ΔEIS is the EIS change in the first or last 30 years of abrupt4xCO2 simulations. The first three terms on the right side of Eq. (3) represent the components of ΔEIS (abrupt4xCO2) driven by FR, UOW and NOW, respectively. They are computed by rescaling $\Delta EIS(FR)$, $\Delta EIS(UOW)$ and $\Delta EIS(NOW)$ with three coefficients, α, β and γ.

The value of α is set to 1. This is a reasonable approximation because the effective radiative forcing in abrupt4xCO2 simulations differs only slightly from the effective radiative forcing in their corresponding amip4xCO2 simulations (Andrews et al. 2012). See Myhre et al. (2013) for a definition of effective radiative forcing, and recall that $\Delta EIS(FR)$ is computed based on amip4xCO2 simulations. The β and γ are computed for each abrupt4xCO2 simulation as tropical SST change for that simulation divided by 4 K (see Table 4). This takes care of the fact that idealized (amip4K and amipFuture) simulations all had approximately 4 K of warming, but abrupt4xCO2 simulations differ in their warming strength. Recall that $\Delta EIS(UOW)$ and $\Delta EIS(NOW)$ are computed based on amip4K and amipFuture simulations, respectively. Here, we compute the NOW term in Eq. (3) by rescaling $\Delta EIS(NOW)$ because the patterns of tropical SST change in these simulations are very similar to the pattern of tropical SST change imposed on the amipFuture simulations. The typical spatial correlation is 0.7 between the tropical SST change in the first or last 30 years of abrupt4xCO2 simulation and the tropical SST change in the corresponding amipFuture simulations.

Table 4 The three scaling factors in decomposing EIS changes in eight abrupt4xCO2 simulations

	α	β	γ	r
First 30 years[1]	1	0.64 ($\pm$0.10)	0.64 ($\pm$0.10)	0.73 ($\pm$0.15)
First 30 years[2]	1.10 ($\pm$0.51)	0.60 ($\pm$0.15)	0.63 ($\pm$0.17)	0.75 ($\pm$0.12)
Last 30 years[1]	1	0.96 ($\pm$0.18)	0.96 ($\pm$0.18)	0.74 ($\pm$0.11)
Last 30 years[2]	1.01 ($\pm$0.59)	0.72 ($\pm$0.20)	0.89 ($\pm$0.25)	0.76 ($\pm$0.09)

First row: The ensemble-mean and cross-model standard deviation of α, β and γ, based on effective radiative forcing and tropical oceanic warming in the first 30 years of eight abrupt4xCO2 simulations. Second row: As in the first row, but for the values of α, β and γ, obtained empirically. Third row: As in the first row, but for the last 30 years. Fourth row: As in the second row, but for the last 30 years. The ensemble-mean and cross-model standard deviation of the correlation between ΔEIS(abrupt4xCO2) and the sum of the first three terms on the right side of Eq. (3) are also shown

[1] and [2] indicate the theoetical and empirical methods to decompose EIS changes

Alternatively, one can quantify the three scaling factors empirically. This can be done by exploiting spatial variability in ΔEIS(abrupt4xCO2). It turns out that $\Delta EIS(FR)$, $\Delta EIS(UOW)$ and $\Delta EIS(NOW)$ all exhibit different spatial patterns (see Sect. 4). So, to tease out the respective contributions of FR, UOW and NOW to ΔEIS(abrupt4xCO2), we regress ΔEIS(abrupt4xCO2) onto $\Delta EIS(FR)$, $\Delta EIS(UOW)$ and $\Delta EIS(NOW)$ within each model. (For each EIS change pattern, EIS changes at all grid points within the tropical ocean are concatenated before the regression analysis.) The three scaling factors assume the respective values of the three regression coefficients. We find that on an ensemble-mean basis, the empirical estimates of the scaling factors are very close to the respective estimates based on effective radiative forcing and tropical warming (see Table 4). This suggests that the EIS change in abrupt4xCO2 simulations can to a very good approximation be viewed as a linear supposition of the EIS change from the effects of FR, UOW and NOW. A noticeable difference between the two approaches is that for the last 30 years, the empirical estimate of β is somewhat less than the β estimate based on tropical warming. We note that there may be inherent uncertainties associated with the empirical estimates of the scaling factors. Particularly, because the tropical SST change patterns in abrupt4xCO2 simulations are not exactly the same as the SST change pattern imposed on amipFuture simulations, the terms of FR, UOW and NOW in the regression model may be aliased by the EIS change due to NOW that cannot be rescaled with $\Delta EIS(NOW)$.

The residual term, $\Delta EIS(Res)$ is calculated as the value that makes the equality in (3) true. It may be driven by the EIS change due to NOW that cannot be rescaled with $\Delta EIS(NOW)$. Again, this portion of EIS change takes place because the tropical SST change patterns in abrupt4xCO2

simulations are not exactly the same as the SST change pattern imposed on amipFuture simulations.

It is not straightforward to decompose $\Delta EIS(RCP8.5)$ using Eq. (3) because the radiative forcing in the 21st-century stems from not only an increase in CO_2, but also increases in other greenhouse gases, as well as changes in aerosol concentration and land use. However, if assuming that the effects of other greenhouse gases on EIS can be scaled with the effect of CO_2, and that the effects of changes in aerosol concentration and land use are small, we can still obtain values of α, β and γ for RCP8.5 simulations. Averaged over eight RCP8.5 simulations, α is close to 0.8, and both β and γ are close to 0.6. These values are comparable to the corresponding values for the first 30 years of abrupt4xCO2 simulations (see Table 4). This similarity may be attributed to two facts: The effective greenhouse gas (GHG) forcing in the 21st-century of RCP8.5 simulations is only slightly less than that in amip4xCO2 simulations (Myhre et al. 2013), and the magnitude of tropical warming is comparable in the 21st-century of RCP8.5 simulations and the first 30 years of abrupt4xCO2 simulations (the ensemble-mean tropical SST change is close to 2.5 K in both cases).

The EIS change in LGM simulations is not decomposed using Eq. (3) for two reasons. First, more than half of the radiative forcing in LGM is driven by changes in the Northern Hemisphere ice sheets, vegetation cover and aerosols (Jansen et al. 2007). It is unclear how EIS responds to these forcings. Second, it is not feasible to quantify the EIS change due to NOW in LGM simulations by rescaling $\Delta EIS(NOW)$. The patterns of tropical SST change in these simulations do not correspond well to the pattern of tropical SST change imposed on amipFuture simulations: The typical spatial correlation between the tropical SST change in LGM simulation and the tropical SST change in the corresponding amipFuture simulation is -0.26.

3 Present-day tropical inversion

We first examine the present-day inversion based on ERA-Interim reanalysis (1979–2008). The geographic distribution of present-day EIS is shown in Fig. 1a. Not surprisingly, large positive EIS values are found in the subtropical oceanic regions off the west coasts of continents. These regions are typically associated with equatorward currents, coastal upwelling and stratocumulus decks. These phenomena altogether maintain a relatively cool ocean and hence a very stable atmospheric boundary layer. Overall, about 40 % of the tropical ocean is occupied by positive EIS values (Table 5). The mean strength of the inversion, defined as average EIS over regions with positive EIS, is about 2 K (Table 5). In comparison, EIS is much higher in the KH
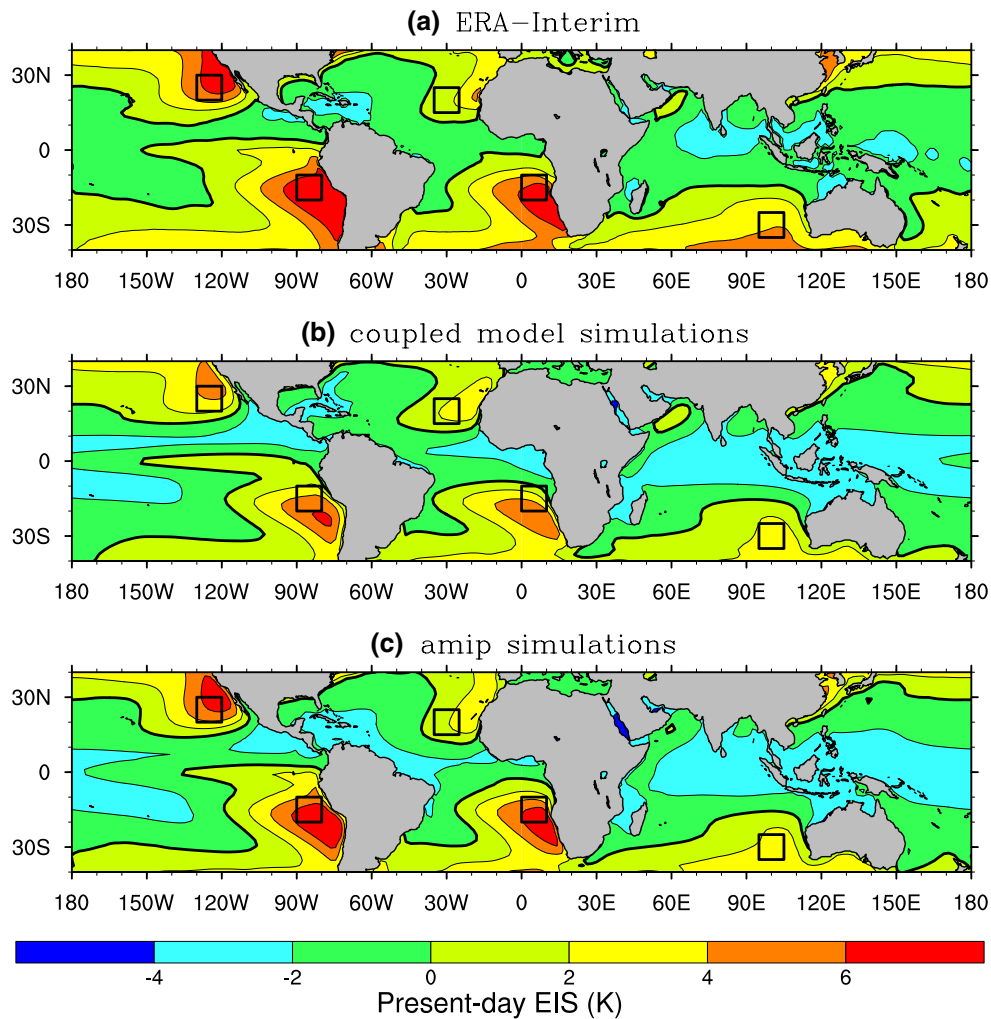
Fig. 1 Geographic distribution of present-day EIS (1979–2008) in both reanalysis and simulations. **a** The ERA-Interim reanalysis. **b** The ensemble-mean of 18 coupled model simulations. **c** The ensemble-mean of 13 amip simulations. The *thick curve in each diagram* represents the zero contour line. The main low cloud regions off the coasts of Peru, Namibia, Australia, California and Canary are represented by *five black boxes* and referred to as the KH domains throughout the paper

Table 5 Areal coverage of the present-day (1979–2008) tropical inversion (*A*), the mean inversion strength (EIS), and the average EIS over the KH domains (EIS_{kh}) in reanalysis and simulations

	ERA-Interim	NCAR/NCEP	MERRA	Coupled model	amip
A	0.42	0.37	0.29	0.31 (±0.11)	0.28 (±0.10)
EIS	2.23	1.86	2.35	1.89 (±0.33)	2.50 (±0.22)
EIS_{kh}	5.02	4.37	4.29	3.18 (±1.20)	4.48 (±0.64)

1st column: Values based on ERA-Interim. 2nd column: Values based on NCAR/NCEP. 3rd column: Values based on MERRA. 4th column: The ensemble-mean of 18 coupled model simulations. 5th column: The ensemble-mean of 13 amip simulations. The cross-model standard deviation of all quantities in columns 4–5 are shown in parentheses. Unit for EIS is K

domains (represented by black boxes in Fig. 1), averaging up to 5 K (Table 5). To assess the uncertainty in reanlysis, we also examine two other reanalysis data sets, NCAR/NCEP and MERRA over the same period (1979–2008). The geographic distribution of present-day EIS based on the two data sets (not shown) is very similar to Fig. 1a. Discrepancy in both inversion coverage and strength is generally less than 20 % among different data sets (Table 5).

The geographic distribution of ensemble-mean present-day EIS in 18 coupled model simulations is shown in Fig. 1b. Coupled models as an ensemble capture the geographic distribution of EIS in reanalysis reasonably well. Nevertheless, simulated EIS is negatively biased near the west coasts of continents. Averaged over the KH domains and the 18
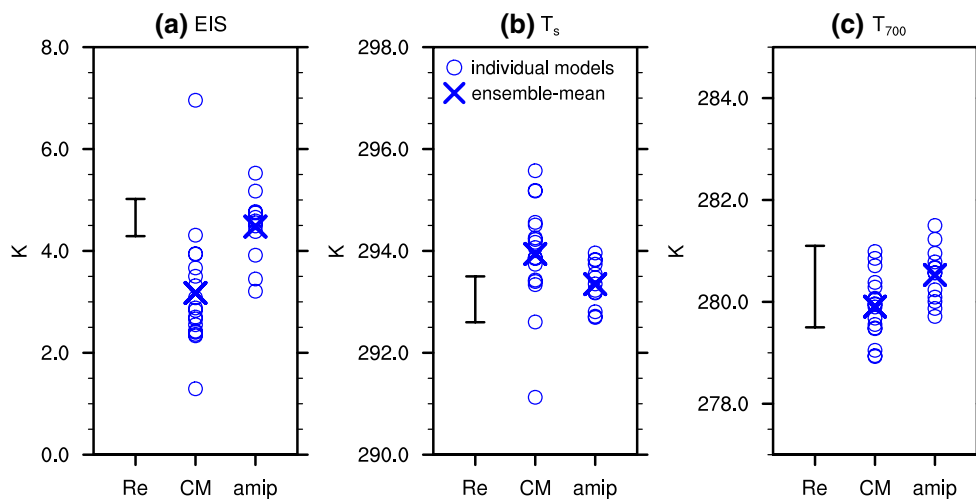
Fig. 2 Various present-day quantities averaged over the KH domains. **a** EIS. **b** T_s. **c** T_{700}. The *error bars* represent the range of each quantity in reanalysis (Re), the *open circles* the individual coupled model (CM) or amip simulations and the cross signs the ensemble-means

models, EIS is only about 3 K (which is 1 K lower than the lower bound of the EIS range suggested by reanalysis, see Table 5; Fig. 2a). This negative bias is systematic and occurs in 16 out of the 18 models (Fig. 2a). To identify the sources of the bias, we compare simulated T_s and T_{700} with the respective quantities in reanalysis. Simulated T_s is greater than the upper bound of the T_s range suggested by reanalysis in 13 out of 18 coupled simulations (Fig. 2b), while simulated T_{700} lies within the T_{700} range suggested by reanalysis in most coupled model simulations (Fig. 2c). Therefore, the negative EIS bias in the coupled model simulations is primarily attributable to the warm bias in T_s. This warm bias is commonly seen at the west coasts of subtropical continents in fully coupled atmosphere-ocean simulations (Zheng et al. 2011; Xu et al. 2013).

To investigate the EIS bias further, we examine 13 amip simulations, AGCM simulations forced by observed SST (see Sect. 2 for detail). We expect T_s, and subsequently EIS to be less biased in these simulations. Figure 1c shows the geographic distribution of ensemble-mean present-day EIS in amip simulations. Consistent with our expectation, EIS off the west coasts of continents is considerably larger in amip simulations than coupled model simulations (comparing Fig. 1b, c). Averaged over the KH domains and the 13 amip simulations, EIS is close to 4.5 K (Table 5). This is about 1 K greater than the ensemble-mean EIS in the 18 coupled model simulations, and is in better agreement with the EIS in reanalysis (Fig. 2a). The EIS bias is reduced in most individual amip simulations as well (Fig. 2a). This reduction is mostly attributable to the fact that T_s is better simulated in amip simulations than in coupled model simulations (Fig. 2b). As for T_{700}, there are no significant differences between the two types of simulations (Fig. 2c). It is worth noting that given the importance of EIS in regulating

LCC, the negative EIS bias may contribute to the low LCC bias in coupled model simulations (Klein et al. 2013). Consistent with this conjecture, the regionally-averaged LCC in the KH domains is greater in 9 of the 13 amip simulations than their respective coupled model simulations (the mean difference in the 9 models is 4.7 %, not shown).

Averaged over all coupled model simulations, the areal coverage of the inversion is 0.31, which is slightly greater than the lower bound of the range suggested by reanalysis (see Table 5). Surprisingly, the areal coverage of the inversion is even lower in amip simulations than in coupled model simulations.

4 EIS change in AGCM simulations

4.1 $\Delta EIS(FR)$

Figure 3a shows the geographic distribution of ensemble-mean $\Delta EIS(FR)$ in the eight AGCMs with necessary data available. The ensemble-mean $\Delta EIS(FR)$ is positive everywhere, but generally less than 0.4 K. In the subtropical Atlantic ocean, however, it can reach up to 0.6 K. Averaged over the eight models, $\Delta EIS(FR)$ increases the areal coverage of inversion by about 0.04, the mean inversion strength by 0.36 K and the average inversion strength over the KH domains by 0.44 K (Table 6). Our estimate of $\Delta EIS(FR)$ due to CO_2 quadrupling is consistent with the estimate in Webb et al. (2012)—a EIS increase of 0.1–0.2 K for CO_2 doubling.

Since SST does not change by construction in the fast response case (Fig. 3b), the positive values of $\Delta EIS(FR)$ are exclusively attributable to the positive values of
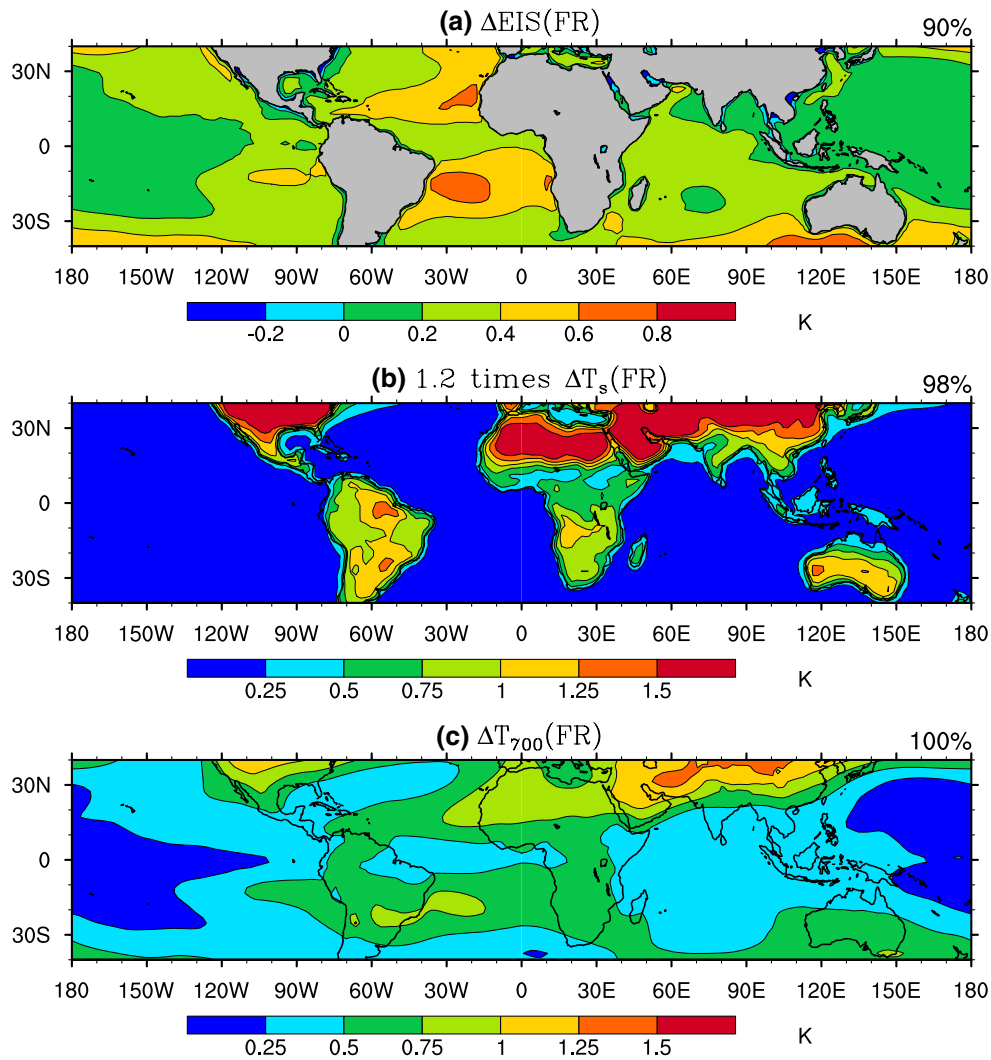
Fig. 3 Geographic distribution of the ensemble-mean fast EIS change and its two components in eight AGCMs. **a** $\Delta EIS(FR)$. **b** $1.2\Delta T_s(FR)$. **c** $\Delta T_{700}(FR)$. In *each diagram*, the portion of grid points within the tropical ocean where the sign of the quantity agrees in at least 7 models is shown at the *upper-right corner*

Table 6 The ensemble-mean changes in the areal coverage of inversion (ΔA), the mean inversion strength (ΔEIS), and the average EIS over the KH domains (ΔEIS_{kh}) due to FR, UOW and NOW in eight AGCMs

	FR	UOW	NOW
ΔA	0.04 (±0.01)	0.07 (±0.03)	0.02 (±0.02)
ΔEIS	0.36 (±0.09)	0.54 (±0.25)	0.39 (±0.25)
ΔEIS_{kh}	0.44 (±0.14)	0.61 (±0.28)	0.38 (±0.28)

The cross-model standard deviations of various changes are shown in parentheses

$\Delta T_{700}(FR)$ (Fig. 3c). An increase in GHG concentration with fixed SST could lead to increases of T_{700} over the ocean through two processes. First, the GHG increase reduces lower tropospheric cooling by trapping more longwave radiation, *in situ*. Second, the GHG increase induces rapid warming over land. Through tropical circulation, this warming could have a remote impact on tropospheric temperature over the ocean, as suggested by the somewhat larger warming at T_{700} over oceanic regions adjacent to land areas.

To assess the relative importance of these two processes, we examine EIS in 6 aquaControl/aqua4xCO2 simulations (see Appendix 2). Averaged over the six simulations, the EIS increase due to CO2 quadrupling is about 0.13 K and largely independent of latitude (Fig. 12). This EIS increase accounts for only 1/3 the ensemble-mean EIS increase in amip4xCO2 simulations (0.36 K). Assuming the difference in the EIS increase between aqua4xCO2 and amip4xCO2 simulations is all attributable to the GHG-induced continental warming, this suggests that about 2/3 of the EIS
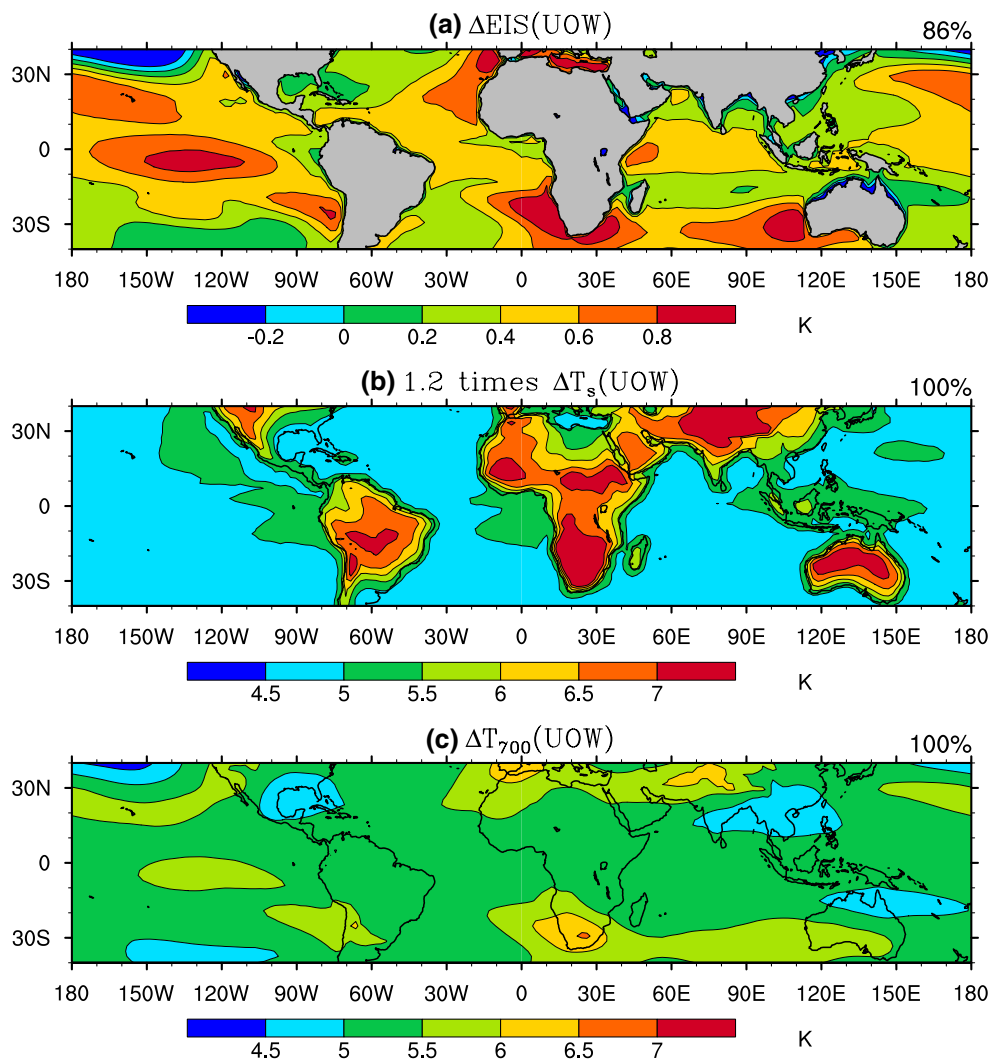
Fig. 4 Geographic distribution of the ensemble-mean EIS change due to uniform oceanic warming and its two components in eight AGCMs. **a** $\Delta EIS(UOM)$. **b** $1.2\Delta T_s(UOM)$. **c** $\Delta T_{700}(UOM)$. In *each* *diagram*, the portion of grid points within the tropical ocean where the sign of the quantity agrees in at least 7 models is shown at the *upper-right corner*

increase in amip4xCO2 simulations (Fig. 3b) may have been induced by the continental warming.

4.2 $\Delta EIS(UOW)$

Figure 4a shows the geographic distribution of ensemble-mean $\Delta EIS(UOW)$ in the eight AGCMs. The ensemble-mean $\Delta EIS(UOW)$ is positive throughout the tropical ocean, with elevated values off the west coasts of continents and in the eastern equatorial Pacific. The positive sign of the ensemble-mean $\Delta EIS(UOW)$ is attributable to the fact that the ensemble-mean $\Delta T_{700}(UOW)$ (Fig. 4c) is larger than the ensemble-mean $1.2\Delta T_s(UOW)$ (Fig. 4b). Averaged over the eight models, $\Delta EIS(UOW)$ increases

the areal coverage of inversion by 0.07, the mean inversion strength by 0.54 K and the average inversion strength over the KH domains by 0.61 K (Table 6).

The EIS change in the six aqua4K simulations is quantified (see Fig. 12c in Appendix 2). Averaged over the tropical ocean and the six simulations, EIS increases by 0.5 K. This is close to the ensemble-mean EIS change in amip4K simulations (Table 6). Our expectation was that the lapse rate in deep convective regions would remain close to the moist adiabat, in which case EIS should not change from amip to amip4K (or aquaControl to aqua4K) simulations. Yet, EIS increases by about 0.5 K in the tropics in both amip4K and aqua4K simulations. Note that this also implies continental warming plays a secondary role in driving the EIS increase in amip4K simulations. To understand
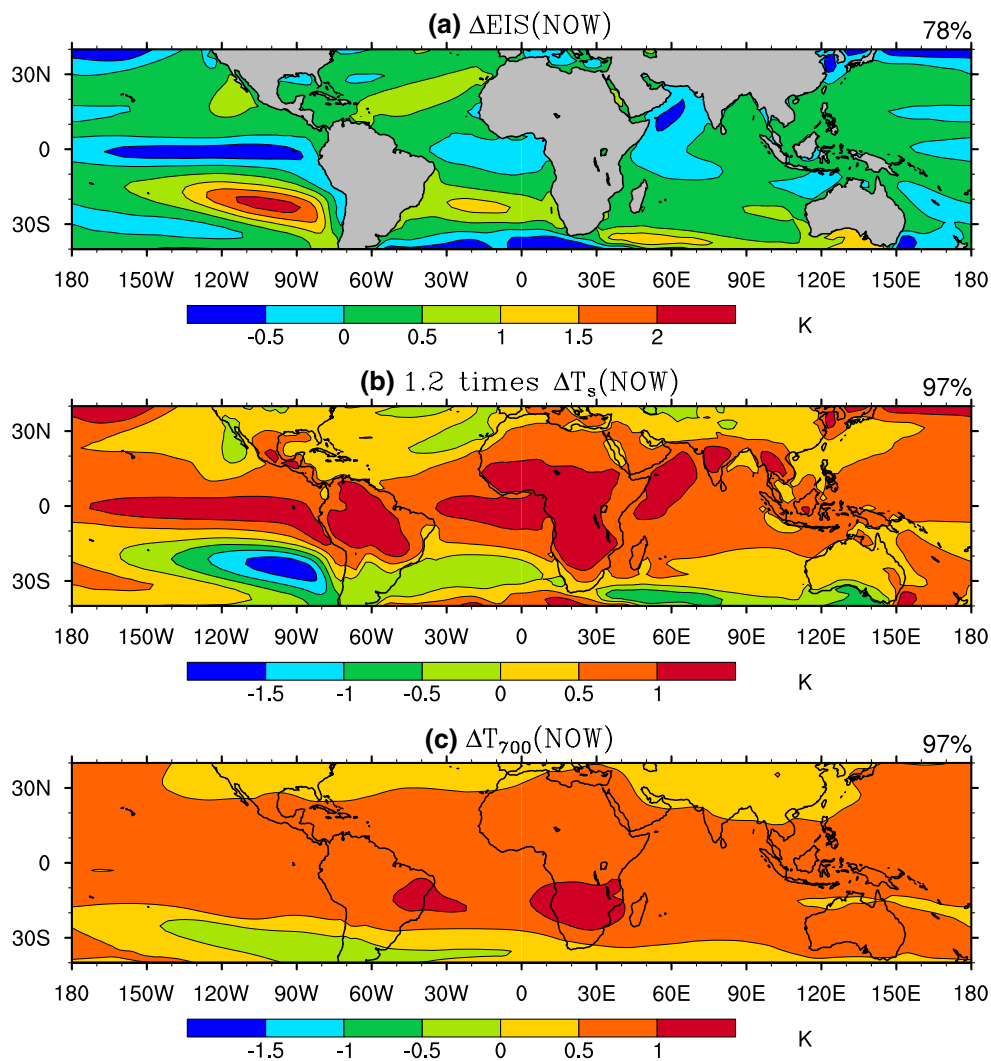
Fig. 5 Geographic distribution of the ensemble-mean EIS change due to nonuniform oceanic warming and its two components in eight AGCMs. **a** $\Delta EIS(NOM)$. **b** $1.2\Delta T_s(NOM)$. **c** $\Delta T_{700}(NOM)$. Note that to get $\Delta EIS(NOM)$, $\Delta T_s(NOM)$ and $\Delta T_{700}(NOM)$, we removed $\Delta EIS(UOM)$, $\Delta T_s(UOW)$ and $\Delta T_{700}(UOW)$ from the overall EIS, T_s and T_{700} changes in amipFuture simulations, respectively. In *each diagram*, the portion of grid points within the tropical ocean where the sign of the quantity agrees in at least 7 models is shown at the *upper-right corner*

which vertical levels deviate most from the moist adiabat, we examine the vertical profile of potential temperature change averaged over the 10S-10N latitude band in the six aqua4K simulations (see Fig. 13 in Appendix 2). While the simulated change in potential temperature generally follows the moist adiabat from the surface to 850 hPa, it is robustly more positive than the moist adiabat between 850 and 600 hPa. This warming aloft greater than the moist adiabat is what drives the EIS increase in the aqua4K simulations. The deviation from the moist adiabat between 850 and 600 hPa may be attributed in part to the increase in humidity throughout the troposphere associated with warming. The humidity increase may reduce lower tropospheric

cooling relative to upper tropospheric cooling by trapping more long wave radiation, *in situ* and thus induce a small warming relative to the moist adiabat in T_{700}.

4.3 $\Delta EIS(NOW)$

The geographic distribution of ensemble-mean $\Delta EIS(NOW)$ in the eight AGCMs is shown in Fig. 5a. The ensemble-mean $\Delta EIS(NOW)$ exhibits more spatial variations than the ensemble-mean $\Delta EIS(FR)$ and $\Delta EIS(UOW)$. It is positive in much of the subtropical ocean (especially the southeast Pacific), and negative in the eastern equatorial Pacific. The positive values of $\Delta EIS(NOW)$ are primarily
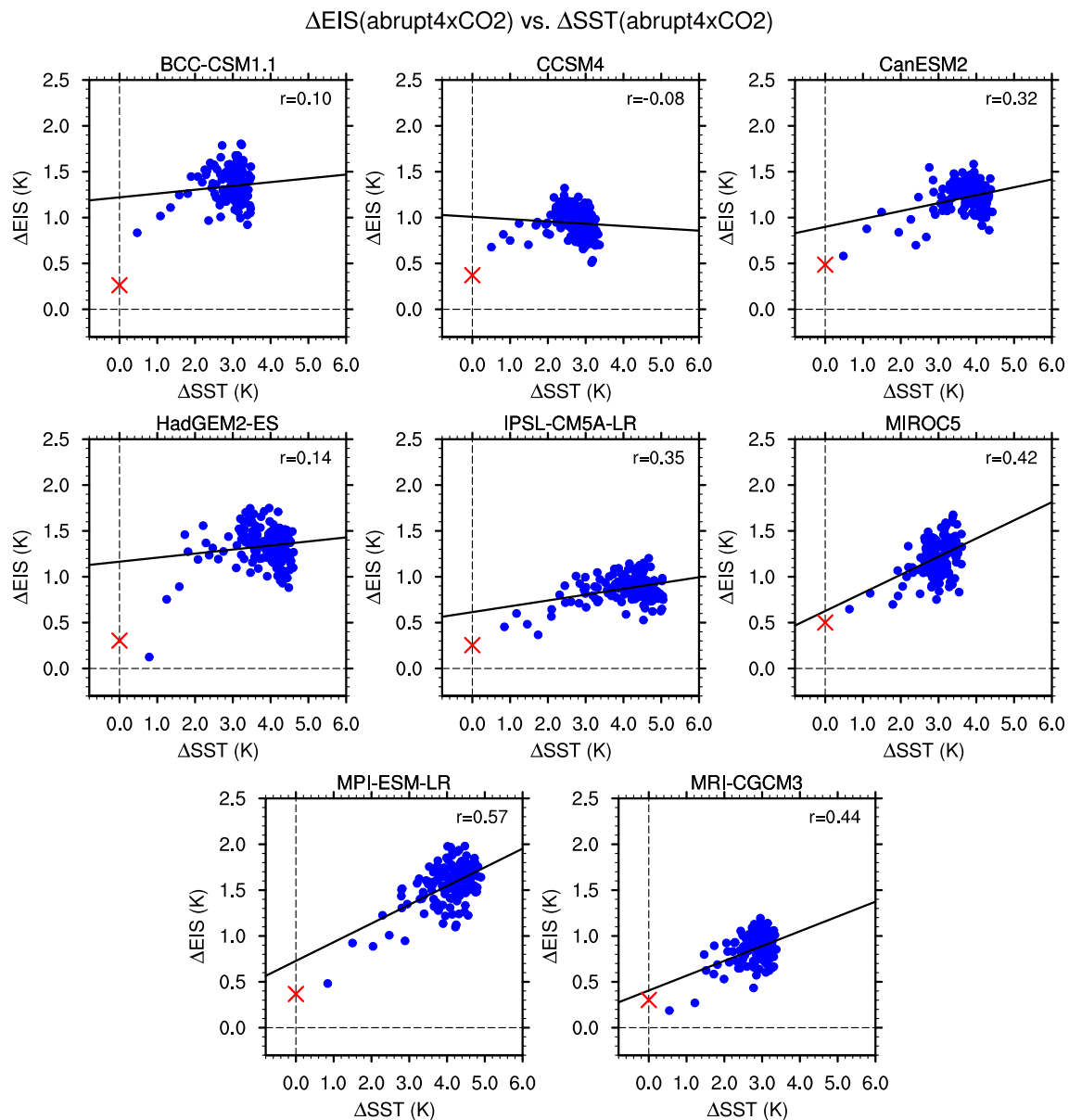
ΔEIS(abrupt4xCO2) vs. ΔSST(abrupt4xCO2)

Fig. 6 Scatterplots of EIS changes averaged over the tropical ocean with inversion versus changes in the tropical SST in 8 abrupt4xCO2 simulations. The *blue dots* represent the yearly changes in EIS and tropical SST in abrupt4xCO2 simulations relative to the respective climatological values in the piControl simulations. The *red crosses* represent changes in the mean inversion strength and tropical SST in amip4xCO2 simulations. Note that by construction there is no change in the tropical SST in amip4xCO2 simulations. The best-fit regression line between the two quantities is also shown in *each diagram*, as well as the correlation between the two quantities

attributed to negative values of $1.2\Delta T_s(NOW)$ (Fig. 5b) and to a lesser extent, the positive values of $\Delta T_{700}(NOW)$ (Fig. 5c), while the negative values of $\Delta EIS(NOW)$ are attributed to the positive values of $1.2\Delta T_s(NOW)$. The spatial variations in $1.2\Delta T_s(NOW)$ can subsequently be attributed to the fact that the subtropical ocean (10–30 S/N) warms less than the equatorial ocean (10S-10N) (see Fig. 5b). Averaged over all models, $1.2\Delta T_s(NOW)$ is 0.5 K less in the subtropical ocean than the equatorial ocean. This

nonuniform warming is robust and occurs in every model. It is attributed in part to differences in local feedbacks between the two regions (Liu et al. 2005; Xie et al. 2010). In contrast, $\Delta T_{700}(NOW)$ is relatively uniform in the tropics, owing to the dynamical constraint of a weak temperature gradient in the tropical free-troposphere.

Averaged over the eight models, $\Delta EIS(NOW)$ increases the areal coverage of the inversion by 0.02, the mean inversion strength by 0.39 K and the average inversion strength
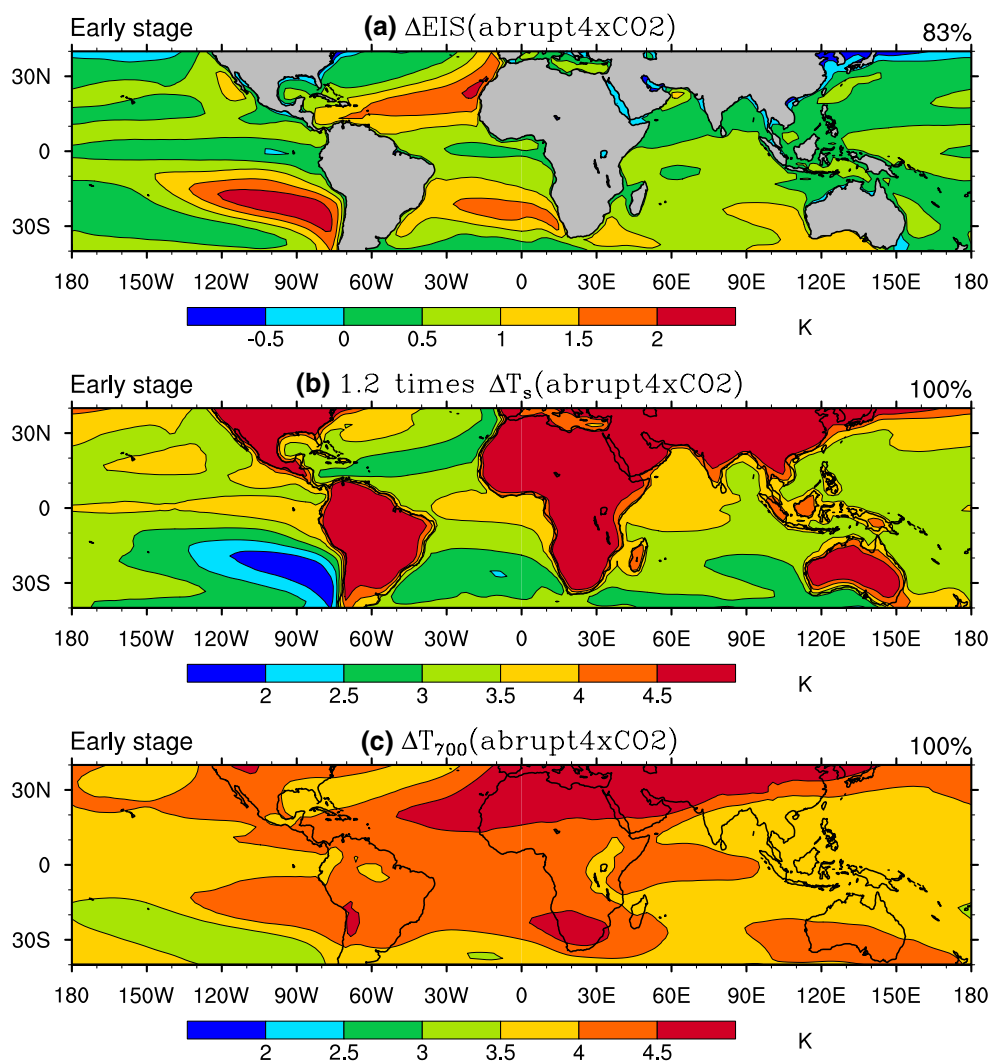
Fig. 7 Geographic distribution of the ensemble-mean EIS change and its two components in the first 30 years of eight abrupt4xCO2 simulations. **a** ΔEIS(abrupt4xCO2). **b** $1.2\Delta T_s$(abrupt4xCO2). **c** ΔT_{700} (abrupt4xCO2). In *each diagram*, the portion of grid points within the tropical ocean where the sign of the quantity agrees in at least 7 models is shown at the *upper-right corner*

over the KH domains by 0.38 K (Table 6). Note that to calculate changes in the inversion coverage due to NOW, we add $\Delta EIS(NOW)$ to simulated present-day EIS and compute the inversion coverage associated with the perturbed EIS field. Then we quantify the difference with present-day inversion coverage. Our estimate of the temperature-mediated EIS change is in good agreement with Webb et al. (2012). According to their work, the CMIP3 ensemble-mean temperature-mediated EIS change normalized by the global-mean temperature change is about 0.1–0.2 K/K (see their Fig. 7e). Using the ensemble-mean values of $\Delta EIS(UOW)$ and $\Delta EIS(NOW)$ as well as the ensemble-mean global-mean temperature change in both amip4K and amipFuture simulations (4.5 K), we estimate the CMIP5 ensemble-mean temperature-mediated EIS change to be 0.2 K/K.

5 EIS change in the coupled model simulations

5.1 Decomposing EIS change

The annual-mean EIS change in 8 abrup4xCO2 simulations is scattered against the corresponding increase in the annual-mean tropical SST in Fig. 6. We find that the EIS changes in many simulations are a nonlinear function of tropical warming: EIS increases rapidly with warming during the first few decades, but stagnates afterwards. This is further supported by the small correlation between the EIS and SST changes in most models. Because of this nonlinearity, the intercept of the best-fit regression line between the two quantities is generally much greater than the estimated fast EIS response based on amip4xCO2 simulations (red crosses in Fig. 6). This suggests that the Gregory et al.

(2004) linear-regression method is not appropriate when the curves are nonlinear.

Figure 7 shows the geographic distribution of ensemble-mean EIS change and associated changes in T_s and T_{700} averaged over the first 30 years of eight abrupt4xCO2 simulations. There are widespread EIS increases in a warming climate. The largest increase occurs primarily in the eastern parts of subtropical oceans, consistent with the small surface warming there (Fig. 7b). In the North Atlantic, the regional EIS increase is further enhanced by a maximum of ΔT_{700}(abrupt4xCO2) that appears related to a strong warming over the North Africa (Fig. 7c). Overall, the spatial variations in the ensemble-mean ΔEIS(abrupt4xCO2) are mostly attributable to the spatial variations in the ensemble-mean ΔT_s(abrupt4xCO2) rather than the spatial variations in the ensemble-mean ΔT_{700}(abrupt4xCO2). Comparison of Figs. 7a and 3, 4 and 5a reveals that the geographic distribution of ΔEIS(abrupt4xCO2) apparently bears more resemblance to the geographic distribution of ensemble-mean ΔEIS(NOW) than those of the ensemble-mean ΔEIS(FR) and ΔEIS(UOW). In the first 30 years of abrupt4xCO2 simulations, the areal coverage of the inversion increases on average by 0.1, and the mean EIS increases by about 1 K for the inversion as a whole as well as the KH domains (Fig. 8; Table 7).

To decompose the EIS change in the first 30 years of abrupt4xCO2 simulations, we quantify the various terms (FR, UOW, NOW and residual) of ΔEIS(abrupt4xCO2) using Eq. (3). Recall that the terms of FR, UOW and NOW are computed by rescaling ΔEIS(FR), ΔEIS(UOW) and ΔEIS(NOW) based on the effective radiative forcing and tropical oceanic warming in abrupt4xCO2 simulations. It turns out that averaged over the 8 models, the three terms make comparable contributions to various inversion changes, while the contribution of the residual term is small (Fig. 8).
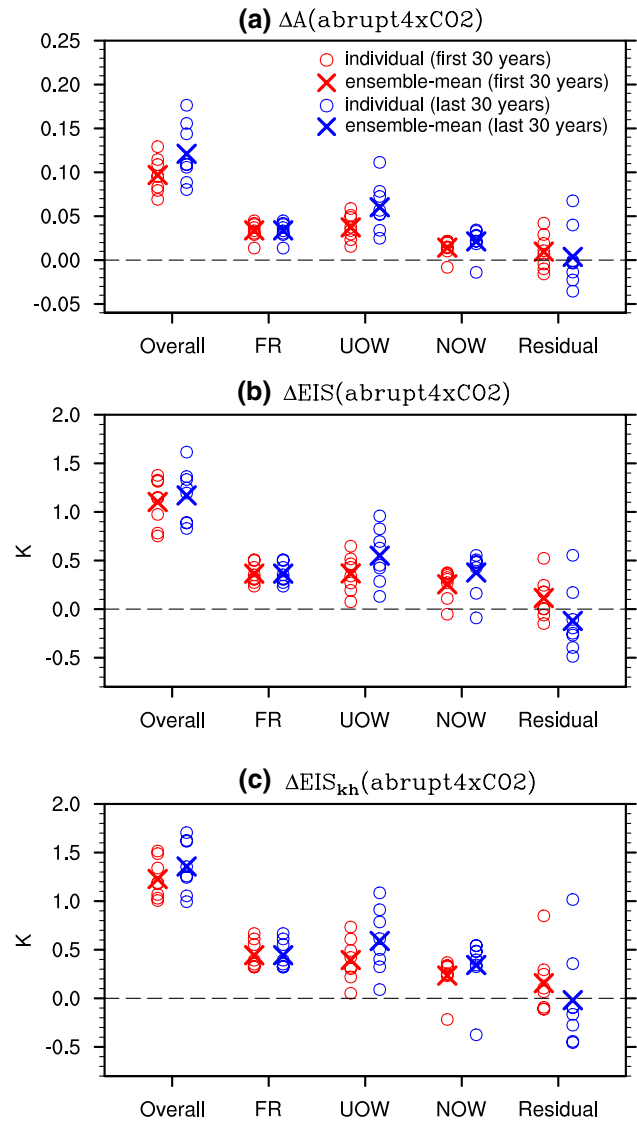

Fig. 8 Changes in the tropical inversion and their four contributors in the first and last 30 years of eight abrupt4xCO2 simulations. **a** Changes in the areal coverage of the tropical inversion (ΔA (abrupt4xCO2)). **b** Changes in the mean inversion strength (ΔEIS (abrupt4xCO2)). **c** Changes in the average EIS over the KH domains (ΔEIS_{kh} (abrupt4xCO2))

The geographic distribution of ensemble-mean EIS change averaged over the last 30 years (years 121–150) of eight abrupt4xCO2 simulations (not shown) is very similar to Fig. 7a. The magnitudes of various inversion changes increase slightly from the first to last 30 years of the simulations (Table 7), due to the increasing magnitudes of UOW and NOW terms in the last 30 years (Fig. 8). The FR term is unchanged because $\alpha = 1$ for both periods (Table 4). On average, the residual term contributes little to changes in the inversion coverage and the average EIS over the KH domains. Nevertheless, it has a small, negative contribution to the mean EIS for the inversion as a whole.
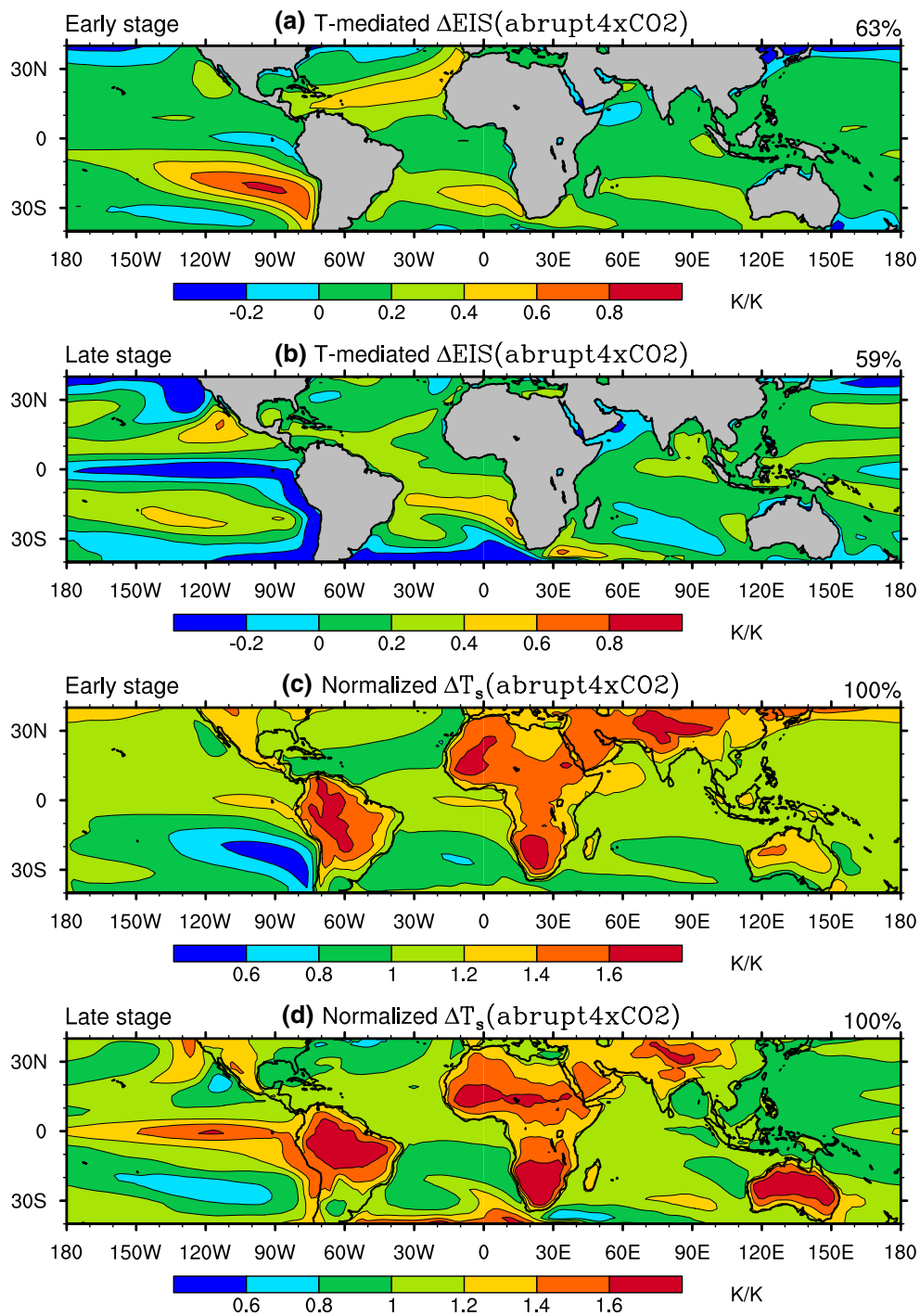
Table 7 The ensemble-mean and cross-model standard deviation of various inversion changes in 8 abrupt4xCO2, 8 RCP8.5 and 4 LGM simulations

	ΔA	ΔEIS	ΔEIS_{kh}
abrupt4xCO2 (first 30 years)	0.10 (±0.02)	1.10 (±0.24)	1.23 (±0.20)
abrupt4xCO2 (last 30 years)	0.12 (±0.03)	1.17 (±0.28)	1.36 (±0.27)
RCP8.5	0.10 (±0.04)	0.86 (±0.23)	0.97 (±0.18)
LGM	0.04 (±0.03)	0.47 (±0.18)	0.58 (±0.36)

1st column: Changes in the areal coverage of inversion (ΔA). 2nd column: Changes in the mean inversion strength (ΔEIS). 3rd column: Changes in the average EIS over the KH domains (ΔEIS_{kh}). Unit for the EIS change is K

Fig. 9 Geographic distribution of the temperature-mediated component of EIS change and associated T_s change in eight abrupt4xCO2 simulations. **a** The temperature-mediated component of EIS change in the first 30 years. **b** The temperature-mediated component of EIS change between the first and last 30 years. **c** Normalized T_s change in the first 30 years. **d** Normalized T_s change between the first and last 30 years. In *each diagram*, the portion of grid points within the tropical ocean where the sign of the quantity agrees in at least 7 models is shown at the *upper-right corner*

5.2 Early versus late EIS change

To understand the nonlinear behavior of the EIS response in abrupt4xCO2 simulations (Fig. 6), we quantify the temperature-mediated EIS changes for the early and late stages of the simulations. For the early stage, we remove the fast EIS response from the overall EIS change averaged over the first 30 years of the simulations. This is
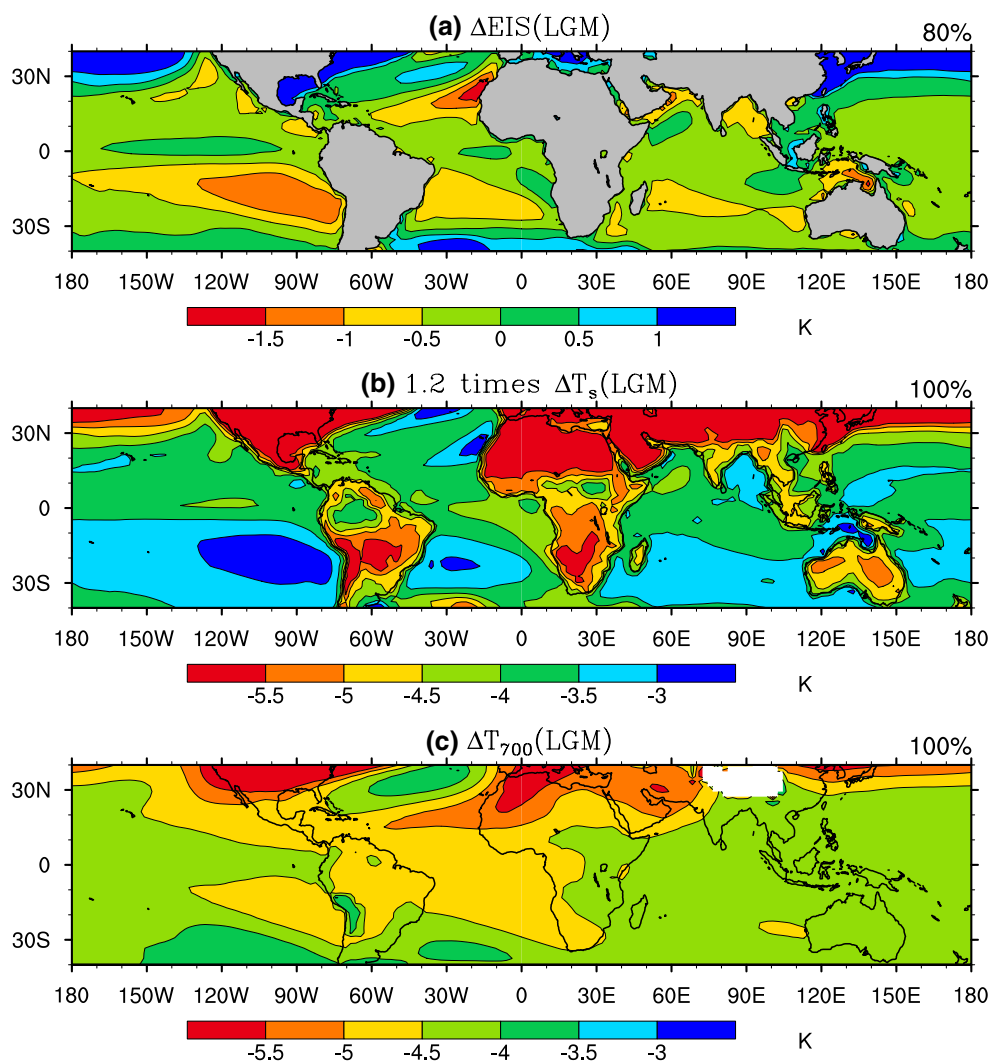
Fig. 10 Geographic distribution of the ensemble-mean EIS change and its two components in four LGM simulations. **a** $\Delta EIS(LGM)$. **b** $1.2\Delta T_s(LGM)$. **c** $\Delta T_{700}(LGM)$. In *each diagram*, the portion of grid points within the tropical ocean where the sign of the quantity agrees in at least 3 models is shown at the *upper-right corner*

equivalent to adding the terms of UOW, NOW and residual for that period altogether (see Fig. 8). For the late stage, we subtract the overall EIS change averaged over the first 30 years from the overall EIS change averaged over the last 30 years. To facilitate comparison, we normalize the temperature-mediated EIS change in the early stage by the tropical SST change averaged over the first 30 years, and normalize the temperature-mediated EIS change in the late stage by the difference in tropical SST change between the first and last 30 years.

The geographic distributions of the ensemble-mean temperature-mediated EIS change in the early and late stages are shown in Fig. 9a, b. We find that the EIS increase is generally much less in the late stage than the early stage. This is especially true in the eastern parts of the subtropical

oceans. In several oceanic regions (e.g., the eastern equatorial Pacific and the Californian region), EIS even decreases in the late stage, in contrast to the early stage when EIS generally increases. Averaged over the tropical ocean with inversion, the ensemble-mean, temperature-mediated EIS change is 0.29 K/K in the early stage and only 0.06 K/K in the late stage (the cross-model standard deviation of temperature-mediated change in the two stages is respectively: 0.09 and 0.08 K/K). Together with the fact that the ensemble-mean tropical SST change is less in the late stage (1.3 K) than in the early stage (2.5 K), this difference accounts for the smaller EIS change in the late stage than in the early stage (see Fig. 6; Table 7).

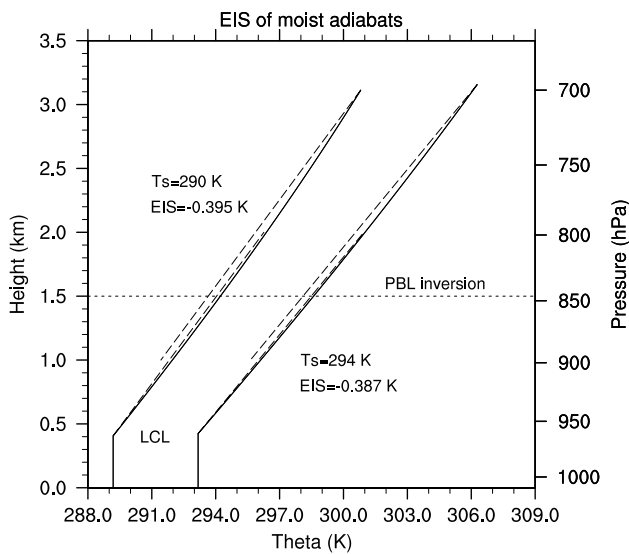The nonlinear EIS response in abrupt4xCO2 simulations may arise from differences in the surface warming

Fig. 11 Two idealized soundings following a dry adiabat below *LCL* and a moist adiabat above it: One represents the present-day climate ($T_s = 290$, the *left solid curve*), and the other represents a warmer climate ($T_s = 294$, the *right solid curve*). In both cases, $p_s = 1,010$ hPa and $RH_s = 80$ %. The EIS values corresponding to the two soundings are calculated using Eq. (1). To illustrate EIS, in each case, we draw *two dashed lines* whose lapse rates are equal to Γ_m^{850}, as defined in Sect. 2. The horizontal distance between the two lines is measured by EIS. The *dotted line* represents the typical height of the inversion base

pattern between the early and late stages of the simulations. To assess this hypothesis, we compare the geographic distribution of the ensemble-mean ΔT_s in the two stages. To facilitate comparison, we normalize ΔT_s in the two stages by the corresponding increase in tropical SST. The geographic distributions of the ensemble-mean, normalized ΔT_s are shown in Fig. 9c, d. Consistent with differences in the EIS change between the two stages, the ensemble-mean T_s change in the eastern parts of the subtropical oceans is generally greater in the late stage than the early stage. Averaged over the tropical ocean with inversion, the ensemble-mean, normalized T_s change is 0.96 K/K in the early stage and 1.12 K/K in the late stage. In contrast, the ensemble-mean, normalized T_{700} change (not shown) is slightly greater in the early stage (1.44 K/K) than the late stage (1.38 K/K). Consistent with this information, a typical spatial correlation of the SST change pattern between amipFuture and abrupt4xCO2 simulations is significantly higher in the early stage (0.70) than the late stage (0.41). Based on these numbers, we conclude that the decreasing rate of EIS increase in the late stage of abrupt4xCO2 simulations is largely driven by delayed warming in the eastern parts of the subtropical oceans relative to the rest of the tropics.
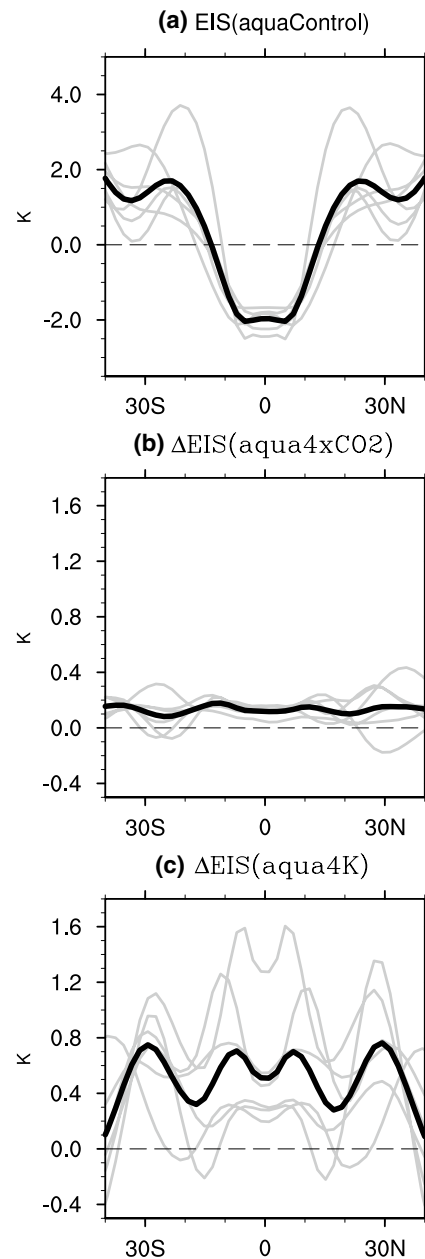

Fig. 12 EIS in aqua simulations. **a** EIS climatology in 6 aquaControl simulations. **b** EIS change in 6 aqua4xCO2 simulations. **c** EIS change in 6 aqua4K simulations. The *gray lines* in each diagram represent individual simulations, while the *black thick line* represents the ensemble-mean

5.3 EIS changes in RCP8.5 and LGM simulations

We also examine EIS changes in 8 RCP8.5 and 4 LGM simulations. The geographic distribution of the ensemble-mean EIS change in 8 RCP8.5 simulations (not shown) is very similar to Fig. 7a. Various inversion changes in
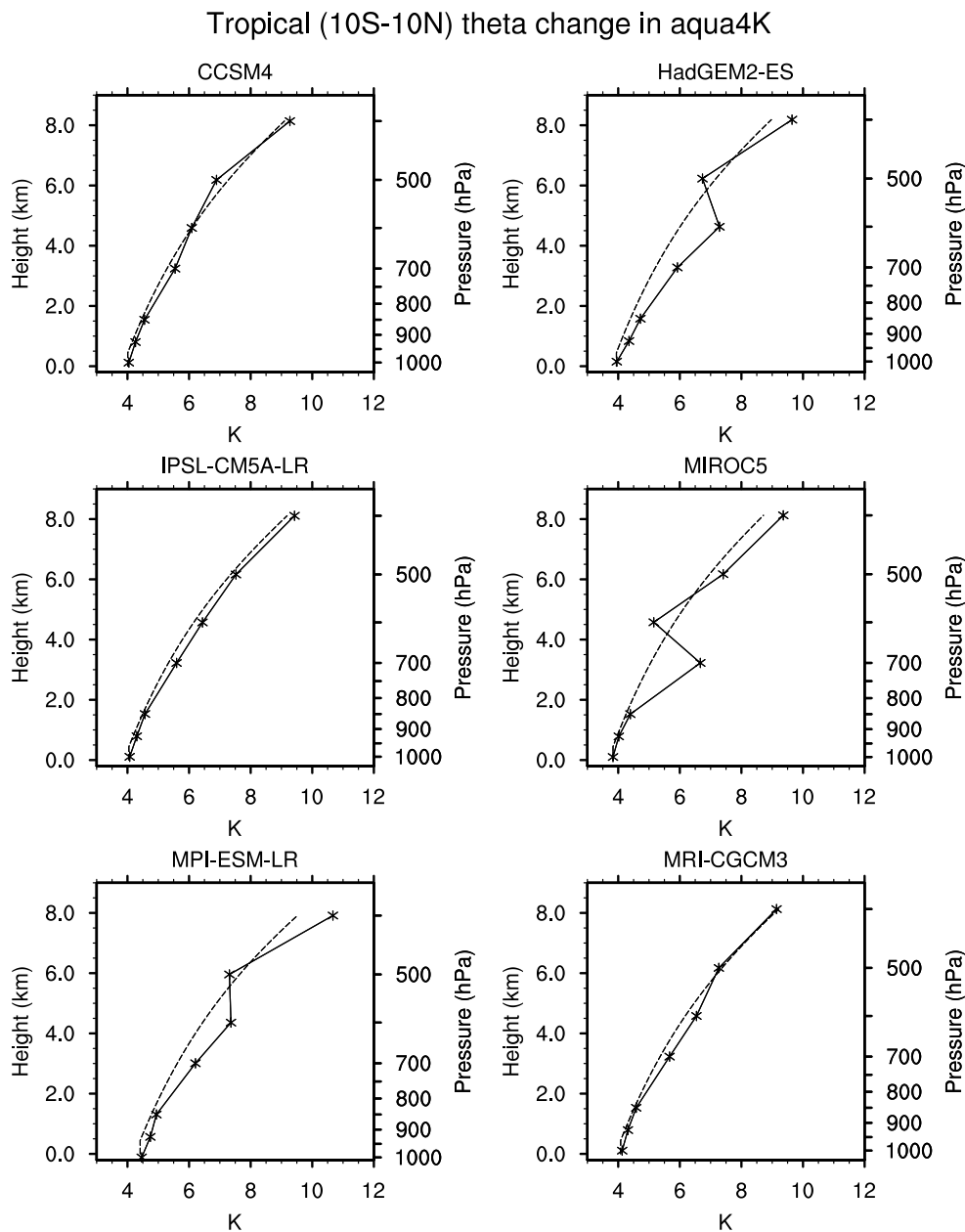
Tropical (10S-10N) theta change in aqua4K

Fig. 13 Vertical profiles of potential temperature change (*solid lines*) in 6 aqua4K simulations relative to their control simulations (aquaControl) averaged over the 10S–10N latitude band. To focus on the regions with deep convection (i.e., those with large upward motion in the mid-troposphere), we weight the potential temperature change by total precipitation (including both convective and non-convective) before spatially averaging it. The corresponding profiles of potential temperature change implied by moist adiabatic lapse rate are also shown for comparison (*dashed lines*). To get these profiles, we first compute the potential temperature at each level in both aquaControl and aqua4K simulations using moist adiabatic lapse rate (see Appendix 1 for detail), as well as simulated sea level pressure and temperature. (Surface relative humidity is fixed at 80 %.) Then, we calculate the difference between the two potential temperatures

RCP8.5 simulations are close to the corresponding quantities in the first 30 years of abrupt4xCO2 simulations (see Table 7). This is also true for different components (FR, UOW, NOW, residual) of the inversion changes (not shown, see discussions in Sect. 2).

The geographic distribution of ensemble-mean EIS change in 4 LGM simulations is shown in Fig. 10a. In contrast to abrupt4xCO2 and RCP8.5 simulations, there are widespread EIS decreases in the cooler climate. The most widespread decrease occurs in the southeast Pacific. Simulated EIS decreases are attributable to the fact that the magnitude of $1.2\Delta T_s$ is less than the magnitude of ΔT_{700} (comparing Fig. 12b, c). Averaged over the four models, the areal coverage of the inversion decreases by 0.04, the

mean EIS decreases by 0.47 K and the average EIS over the KH domains decrease by 0.58 K (Table 7).

Finally, it is worth noting that while the sign of EIS change in both AGCM and coupled model simulations is largely consistent, the magnitude of the change varies a great deal from model to model (see the cross-model standard deviation of various EIS changes in Tables 6, 7; Fig. 8). To assess if the magnitude of simulated EIS change is somehow linked to models' realism in simulating present-day EIS, we compute the cross-model correlation between simulated present-day EIS and EIS change in the KH domains. The correlation turns out to be very small (r ≈ −0.1 for both early and late stages of abrupt4xCO2 simulations), suggesting that the dynamics underpinning simulated EIS change are not closely related to the dynamics shaping performance in simulating present-day EIS.

6 Summary and discussion

In this study, we examine EIS in the tropical marine atmosphere and its response to climate change simulated in 18 CMIP5 models. While CMIP5 models as an ensemble capture the geographic distribution of observed EIS reasonably well, they systematically underestimate present-day EIS off the west coasts of subtropical continents. Averaged over the KH domains and all models, the EIS bias is close to 1 K. This bias is largely attributable to the positive SST bias commonly seen in the fully coupled atmosphere-ocean simulations. Given the importance of EIS in regulating LCC, the negative EIS bias may also contribute to the low LCC bias in climate model simulations.

Using idealized simulations done with AGCMs, we demonstrate that EIS increases in response to anthropogenic forcing in absence of oceanic warming (FR) or oceanic warming in absence of anthropogenic forcing (UOW or NOW). Different mechanisms are responsible for the different EIS increases: The fast EIS increase is strongly impacted by the GHG-induced continental warming via tropical circulation. The UOW contribution is due to warming aloft greater than the moist adiabat in tropical warm pools. The NOW contribution is attributed to the fact that the warm pools warm more than the subtropical ocean.

EIS also increases in coupled model simulations (abrupt4xCO2 and RCP8.5), due to both fast and temperature-mediated EIS changes. Both UOW and NOW contribute to the temperature-mediated EIS change in these simulations. In abrupt4xCO2 simulations, the temperature-mediated EIS change varies with tropical warming in a nonlinear fashion: The EIS increase per degree tropical warming in the early stage of the simulations is almost five times the respective change in the late stage of the simulations, due to delayed warming in the eastern parts of the
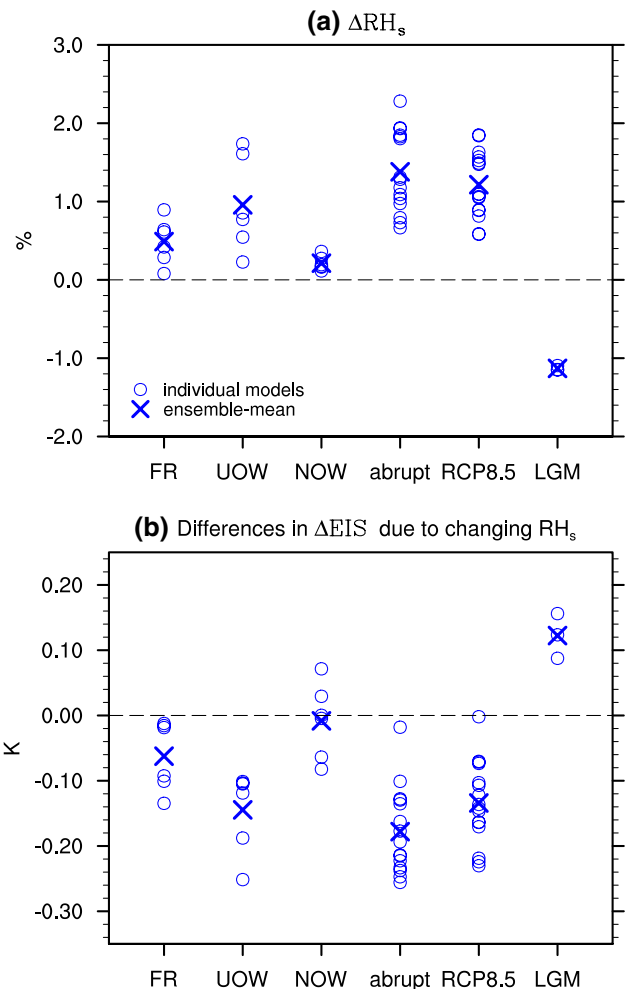

Fig. 14 Changes in surface relative humidity and their influence on simulated EIS change in tropical oceanic area with positive EIS values. **a** The RH_s change in various simulations including 6 amip4xCO2 (FR), 6 amip4K (UOW), 6 ampiFuture (NOW), 15 abrupt4xCO2 (abrupt), 16 RCP8.5 and 3 LGM. The RH_s change due to FR and UOW is with respect to the corresponding amip simulation, the change due to NOW is with respect to the corresponding amip4K simulation, the change in abrupt4xCO2 simulation is with respect to the corresponding piControl simulation and was averaged over the first 30 years of abrupt4xCO2 simulation, the change in RCP8.5 simulation is between the periods 1979–2008 and 2070–2099, and the change in LGM simulation is with respect to present-day. **b** Differences in simulated EIS change due to changing RH_s. To obtain them, we first re-compute various EIS changes using simulated RH_s rather than 80 %. Then we quantify the difference between the new estimates of EIS changes and the original ones

subtropical oceans. Systematic decreases in the inversion coverage and strength are seen in the LGM simulations, suggesting that changes in the tropical inversion are symmetric with respect to the sign of climate change.

An issue which has not been discussed yet is that our estimates of the inversion changes are somewhat sensitive to an underlying assumption in deriving EIS: Surface relative humidity holds to a constant value (80 %). A small,

but systematic increase in this quantify is seen across the tropical ocean in a variety of climate warming simulations, while a small, but systematic decrease is seen in LGM simulations. Accounting for these changes in EIS calculations reduces estimated EIS changes by about 20 %. (See Appendix 3 for detail.) Several aspects of the EIS behavior have not yet been fully understood, including (1) what drives the deviation from the moist adiabat in the warm pools, (2) what processes are most responsible for the uneven warming between the warm pools and the subtropical ocean, and (3) what drives the intermodel spread in the magnitude of EIS increase. Further work is necessary to answer these questions, and to have confidence in the model projections of EIS increase.

Another key question is how LCC would respond to the future EIS increase. Given the strong link between LCC and EIS, LCC ought to increase. One study by Caldwell et al. (2012) supports this view. In their study, imposing CMIP3-model-simulated large-scale changes on a mixed layer model yields an increase in LCC. They attributed this increase primarily to the EIS increase. Furthermore, increases in EIS cause LCC to increase (albeit less strongly than observed) in many fully coupled atmosphere-ocean models (CMIP3 and CMIP5, see Qu et al. 2014). Nevertheless, LCC changes in those models are less impacted by the EIS increase than they are by other cloud controlling factors (e.g., an increase in SST). A recent study using Large-Eddy Simulations also concludes that the EIS rise may be less important to the overall LCC change than other factors, namely the increases in moisture transport through the boundary layer which are fundamentally tied to the warmer temperature in the boundary layer (Bretherton and Blossey 2014). Even so, the EIS change may still play a significant role in coupled model simulations at least in two ways. First, it may contribute to the fast cloud response and thus modulate effective GHG radiative forcing (see Webb et al. 2012). Second, due to its intrinsic nonlinearity, the EIS change may contribute to the nonlinearity of the tropical low-cloud feedback (see Williams et al. 2008 and Andrews et al. 2012). Finally, it is worth noting that the strategy of using idealized AGCM simulations to understand the behavior of coupled model simulations may also be useful to study physical changes other than those in EIS.

Appendix 1: EIS of moist adiabats

While the moist-adiabatic potential temperature gradient, Γ_m is function of temperature and pressure, a single value is used in defining EIS (see Sect. 2). To assess the bias associated with this assumption, we construct an idealized sounding using typical values for surface temperature (290 K), sea level pressure (1,010 hPa) and relative humidity (80 %). The lapse rate of the sounding is dry adiabatic below the *LCL* and moist adiabatic above it (the left solid curve, Fig. 11). While there is no inversion in this sounding, the corresponding EIS is 0.4 K. This suggests that EIS is a negatively biased estimate of inversion strength.

To assess whether this bias is systematic, we construct another idealized sounding, in which we increase the surface temperature by 4 K, while keeping sea level pressure and relative humidity unchanged (the right solid curve, Fig. 11). We find that EIS in this sounding differs little from that in the original sounding. This suggests that the bias in EIS is systematic and similar for a reasonably large range of temperature values. Therefore, it introduces very little bias to the EIS changes examined in this study. It is worth noting that if the temperature profile follows the solid lines in both the present-day and warmer climates, the difference in 700 hPa potential temperature between the two climates is about 1.3 times the difference in surface potential temperature.

Appendix 2: EIS in aqua simulations

The climatological zonal-mean EIS in the 6 aquaControl simulations (gray lines) is shown in Fig. 12a. It is generally positive poleward of 15 degrees. Averaged over the six simulations, the areal coverage of the inversion in the region 30S-30N is 0.53, and the mean inversion strength is 1.33 K. Fig. 12b shows the EIS change in the 6 aqua4xCO2 simulations (gray lines). In at least 4 of the 6 models, positive EIS changes are seen at all latitudes. Averaged over the six simulations, the EIS increase is about 0.13 K and largely independent of latitude, with a large intermodel spread near 30S/N. Figure 12c shows the EIS change in the six aqua4K simulations. Broad EIS increases are also seen in these simulations, albeit with significant intermodel spread. Averaged over the six simulations, EIS change ranges from 0.3 to 0.8 K, with the tropical mean of 0.5 K.

Figure 13 shows the vertical profile of potential temperature change averaged over the 10S-10N latitude band in the six aqua4K simulations. While simulated change in potential temperature generally follows the moist adiabat (dashed lines) from the surface to 850 hPa, it is robustly more positive than the moist adiabat between 850 and 600 hPa.

Appendix 3: Role of changing RH_s

Surface relative humidity assumes a constant value (80 %) in all EIS calculations done so far. However, climate simulations suggest that RH_s changes somewhat in climate change (Richter and Xie 2008). To assess whether these changes significantly affect estimated EIS change, we first examine the RH_s in the various perturbation experiments analyzed in this study (Fig. 14a). Positive RH_s changes are seen in all warming experiments, while negative changes are seen in LGM simulations. The ensemble-mean RH_s change in the warming experiments ranges from 0.2 to 1.5 %, while it is close to 1 % in LGM simulations. There is a large spread across models in the RH_s increase within a particular warming experiment.

Figure 14b shows the difference in simulated EIS change due to changing RH_s. We find that the RH_s increase reduces simulated EIS increase in the warming experiments, while the RH_s decrease reduces simulated EIS decrease in LGM simulations. This is consistent with our expectation because an increase in RH_s tends to reduce LCL and a decrease in RH_s tends to increase LCL (see Eq. (1)). Note that in the case of NOW, the RH_s increase has no systematic effect on simulated EIS change. Averaged over models within each simulation type, the RH_s-induced difference in EIS change is generally less than 20 % of estimated EIS change with fixed RH_s (see Tables 6, 7; Figs. 8, 14b). Note that similar reductions in the EIS change also occur in the aqua4xCO2 and aqua4K simulations, which contribute up to 30 % of the additional warming at T_{700} (relative to the moist adiabat) seen in Fig. 13 (not shown).

References

Andrews T, Gregory JM, Webb MJ, Taylor KE (2012) Forcing, feedbacks and climate sensitivity in CMIP5 coupled atmosphere–ocean climate models. Geophys Res Lett 39:L09712. doi:10.1029/2012GL051607

Betts AK (1997) The physics and parameterization of moist atmospheric convection, chapter 4: trade cumulus: observations and modelling. Kluwer, Dordrecht

Bony S, Dufresne JL (2005) Marine boundary layer clouds at the heart of tropical cloud feedback uncertainties in climate models. Geophys Res Lett 32:L20806. doi:10.1029/2005GL023851

Bretherton CS, Blossey PN (2014) Low cloud reduction in a greenhouse-warmed climate: results from Lagrangian LES of a subtropical marine cloudiness transition. J Adv Model Earth Syst. doi:10.1002/2013MS000250

Caldwell PM, Zhang Y, Klein SA (2012) CMIP3 subtropical stratocumulus cloud feedback interpreted through a mixed-layer Model. J Clim 26:1607–1625

Chen J, Rossow WB, Zhang Y (2000) Radiative effects of cloud-type variations. J Clim 13:264–286

Dee DP et al (2011) The ERA-Interim reanalysis: configuration and perfor-mance of the data assimilation system. Q J R Meteorol Soc 137:553–597

Gregory JM et al (2004) A new method for diagnosing radiative forcing and climate sensitivity. Geophys Res Lett 31:L03205. doi:10.1029/2003GL018747

Hartmann DL, Ockert-Bell ME, Michelsen ML (1992) The effect of cloud type on earth's energy balance: global analysis. J Clim 5:1281–1304

Jansen E et al (2007) Palaeoclimate. In: Solomon S, Qin D, Manning M, Chen Z, Marquis M, Averyt KB, Tignor M, Miller HL (eds) Climate change 2007: the physical science basis. Contribution of working group I to the fourth assessment report of the intergovernmental panel on climate change. Cambridge University Press, Cambridge

Kalnay E et al (1996) The NCEP/NCAR 40-year reanalysis project. Bull Am Meteorol Soc 77:437–470

Klein SA, Hartmann DL (1993) The seasonal cycle of low stratiform clouds. J Clim 6:1587–1606

Klein SA, Zhang Y, Zelinka MD, Pincus RN, Boyle J, Gleckler PJ (2013) Are climate model simulations of clouds improving? An evaluation using the ISCCP simulator. J Geophys Res 118:1–14. doi:10.1002/jgrd.50141

Kubar TL, Waliser DE, Li J-L, Jiang X (2012) On the annual cycle, variability, and correlations of oceanic low-topped clouds with large-scale circulation using Aqua MODIS and ERA-Interim. J Clim 25:6152–6174. doi:10.1175/JCLI-D-11-00478.1

Liu Z, Vavrus S, He F, Wen N, Zhong Y (2005) Rethinking tropical ocean response to global warming: the enhanced equatorial warming. J Clim 18:4684–4700

Moeng CH, Stevens B (1999) Marine stratocumulus and its representation in GCMs. In: Randall DA (ed) General circulation model development: past, present, and future. Elsevier, New York, pp 577–604

Myhre G et al (2013) Anthropogenic and natural radiative forcing. In: Stocker TF, Qin D, Plattner G-K, Tignor M, Allen SK, Boschung J, Nauels A, Xia Y, Bex V, Midgley PM (eds) Climate change 2013: the physical science basis. Contribution of working group I to the fifth assessment report of the intergovernmental panel on climate change. Cambridge University Press, Cambridge

Ogura T, Webb MJ, Watanabe M, Lambert FH, Tsushima Y, Sekiguchi M (2013) Importance of instantaneous radiative forcing for rapid tropospheric adjustment. Clim Dyn. doi:10.1007/s00382-013-1955-x

Qu X, Hall A, Klein SA, Caldwell PM (2014) On the spread of changes in marine low cloud cover in climate model simulations of the 21st century. Clim Dyn 42:2603–2626. doi:10.1007/s00382-013-1945-z

Richter I, Xie S-P (2008) Muted precipitation increase in global warming simulations: a surface evaporation perspective. J Geophys Res 113:D24118. doi:10.1029/2008JD010561

Rienecker MM et al (2011) MERRA: NASA's modern-era retrospective analysis for research and applications. J Clim 24:3624–3648

Slingo A (1990) Sensitivity of the earth's radiation budget to changes in low clouds. Nature 343:49–51

Slingo JM (1980) A cloud parameterization scheme derived from GATE data for use with a numerical model. Q J R Meteorol Soc 106:747–770

Soden BJ, Held IM (2006) An assessment of climate feedbacks in coupled ocean–atmosphere models. J Clim 19:3354–3360

Stephens GL (2005) Cloud feedbacks in the climate system: a critical review. J Clim 18:237–273

Stevens B (2005) Atmospheric moist convection. Annu Rev Earth Planet 33:605–643

Sun F, Hall A, Qu X (2011) On the relationship between low cloud variability and lower tropospheric stability in the Southeast Pacic. Atmos Chem Phys 11:9053–9065. doi:10.5194/acp-11-9053-2011

Taylor KE, Stouffer RJ, Meehl GA (2012) An overview of CMIP5 and the experiment design. Bull Am Meteorol Soc 93:485–498

Vial J, Dufresne JL, Bony S (2013) On the interpretation of inter-model spread in CMIP5 climate sensitivity estimates. Clim Dyn 41:3339–3362. doi:10.1007/s00382-013-1725-9

Watanabe M et al (2012) Fast and slow timescales in the tropical low-cloud response to increasing CO_2 in two climate models. Clim Dyn 39:1627–1641. doi:10.1007/s00382-011-1178-y

Webb MJ, Lambert FH, Gregory JM (2012) Origins of differences in climate sensitivity, forcing and feedback in climate models. Clim Dyn. doi:10.1007/s00382-012-1336-x

Williams KD et al (2006) Evaluation of a component of the cloud response to climate change in an intercomparison of climate models. Clim Dyn 26:145–165

Williams KD, Ingram WJ, Gregory JM (2008) Time variation of effective climate sensitivity in GCMs. J Clim 21:5076–5090. doi:10.1175/2008JCLI2371.1

Wood R, Bretherton CS (2006) On the relationship between stratiform low cloud cover and lower-tropospheric stability. J Clim 19:6425–6432

Wood R (2012) Stratocumulus clouds: review. Mon Weather Rev 140:2373–2423

Wyant MC, Khairoutdinov M, Bretherton CS (2006) Climate sensitivity and cloud response of a GCM with a superparameterization. Geophys Res Lett 33:L06714. doi:10.1029/2005GL025464

Xie S-P, Deser C, Vecchi GA, Ma J, Teng H, Wittenberg AT (2010) Global warming pattern formation: sea surface temperature and rainfall. J Clim 23:966–986. doi:10.1175/2009JCLI3329.1

Xu Z, Li M, Patricola CM, Chang P (2013) Oceanic origin of southeast tropical Atlantic biases. Clim Dyn. doi:10.1007/s00382-013-1901-y

Yue Q, Kahn BH, Fetzer EJ, Teixeira J (2011) Relationship between marine boundary layer clouds and lower tropospheric stability observed by AIRS, CloudSat, and CALIOP. J Geophy Res 116:D18212. doi:10.1029/2011JD016136

Zelinka MD, Klein SA, Hartmann DL (2012) Computing and partitioning cloud feedbacks using cloud property histograms. Part II: attribution to changes in cloud amount, altitude, and optical depth. J Clim 25:3736–3754

Zhang Y, Stevens B, Medeiros B, Ghil M (2009) Low-cloud fraction, lower-tropospheric stability, and large-scale divergence. J Clim 22:4827–4844

Zheng Y, Shinoda T, Lin J-L, Kiladis GN (2011) Sea surface temperature biases under the stratus cloud deck in the southeast Pacific ocean in 19 IPCC AR4 coupled general circulation models. J Clim 24:4139–4164